

The Chemical Homogeneity of Single-Lined Spectroscopic Binaries in Open Clusters

Amaya Sinha,^{1*} Gail Zasowski,¹ Natalie R. Myers,^{2,3} Catherine Manea,^{1†} Peter Frinchaboy,² Katia Cunha,^{4,5} Johanna Müller-Horn,⁶ Yao-Yuan Mao,¹ Aida Behmard,^{7,8} Joleen Carlberg,⁹ Julio Chanamé,¹⁰ Polly Frazer¹¹ Emily Griffith,^{12‡} Sarah Loebman,¹³ A. Roman-Lopes,¹⁴ Jonah Otto,² Diogo Souto¹⁵ Keivan Staussan,¹⁶ Guy S. Stringfellow¹²

¹*Department of Physics and Astronomy, University of Utah, Salt Lake City, UT, 84112, USA*

²*Department of Physics & Astronomy, Texas Christian University, Fort Worth, TX 76129, USA*

³*Department of Physics and Astronomy, Johns Hopkins University, Baltimore, MD 21218, USA*

⁴*Steward Observatory, University of Arizona, Tucson, AZ 85721, USA*

⁵*Observatório Nacional, Rua General José Cristino, 77, 20921-400 São Cristóvão, Rio de Janeiro, RJ, Brazil*

⁶*Max-Planck-Institut für Astronomie, Königstuhl 17, 69117 Heidelberg, Germany*

⁷*Center for Computational Astrophysics, Flatiron Institute, 162 Fifth Avenue, New York, NY 10010, USA*

⁸*American Museum of Natural History, 200 Central Park West, Manhattan, NY 10024, USA*

⁹*Space Telescope Science Institute, 3700 San Martin Drive, Baltimore, MD 21218, USA*

¹⁰*Instituto de Astrofísica, Pontificia Universidad Católica de Chile, Av. Vicuña Mackenna 4860, 782-0436 Macul, Santiago, Chile*

¹¹*Center for Cosmology and Particle Physics, Department of Physics, New York University, 726 Broadway, New York, NY 10003, USA*

¹²*Center for Astrophysics and Space Astronomy, Department of Astrophysical and Planetary Sciences, University of Colorado, 389 UCB, Boulder, CO 80309-0389, USA*

¹³*Department of Physics, University of California, Merced, 5200 Lake Road, Merced, CA 95343, USA*

¹⁴*Department of Astronomy, Universidad de La Serena, Av. Raul Bitran 1302, La Serena, Chile*

¹⁵*Departamento de Física, Universidade Federal de Sergipe, Av. Marechal Rondon, S/N, 49000-000 São Cristóvão, SE, Brazil*

¹⁶*Department of Physics and Astronomy, Vanderbilt University, Nashville, TN 37235, USA*

Accepted XXX. Received YYY; in original form ZZZ

ABSTRACT

Using SDSS-V DR19 Milky Way Mapper APOGEE data, we measure the impact that close binarity has on surface chemistry across the Hertzsprung–Russell diagram in a broad set of abundances by studying single-lined spectroscopic binaries (SB1s) in open clusters. We derive binary membership and orbital parameters for 103 SB1s by analysing APOGEE radial velocities with THE JOKER and ULTRANEST. We perform a detailed abundance analysis with BACCHUS to derive abundances in fourteen chemical species: Si, Fe, C, N, O, Na, Mg, Al, Ca, Ti, Cr, Ni, Ce, and Nd. Leveraging the assumptions of chemical homogeneity in open clusters, we compare the surface abundances of SB1s to non-binary stars at similar evolutionary states. We find that a subset of binaries with significant UV excess have a $\Delta[\text{C/N}]$ that is 0.2–0.5 dex higher than expected, resulting in overestimated [C/N]-based ages for those stars. This points to pollution from an evolved companion and has implications for [C/N]-based age studies of the broader Milky Way. At the population level, we find that SB1s in our sample can be treated as statistically chemically homogeneous with their single-star counterparts, and we find no connection between orbital separation and chemical enrichment or depletion. We show that at separations up to 5 pc, co-eval stars can be considered chemically homogeneous with one another within current abundance precisions, regardless of multiplicity.

Key words: binaries: spectroscopic – stars: abundances – Galaxy: open clusters and associations: general

1 INTRODUCTION

Two stars, both alike in chemistry? Understanding the interplay between stellar multiplicity and evolution is key to understanding not just the life cycles of stars, but also the primary chemical enrichment methods that populate galaxies and the broader universe with heavy elements.

* E-mail: u1363702@utah.edu

† NSF Astronomy and Astrophysics Postdoctoral Fellow

‡ NASA Hubble Fellow

While the Sun lacks a stellar companion, many stars in our Galaxy exist in binaries or higher order systems, and at solar metallicity this fraction is between 10–30% (Offner et al. 2023; Moe et al. 2019; Geller et al. 2021). For OB-type stars this fraction approaches unity (Offner et al. 2023). With some exceptions, binaries and higher-order systems form co-natally, i.e., from the same molecular gas cloud at the same time (Duchêne & Kraus 2013). This makes them a useful tracer for many of the same properties as open clusters, such as studying birth chemistry.

Due to their large separations, wide binaries are often resolvable on the sky as independent sources (e.g., Offner et al. 2010; El-Badry et al. 2021). It is expected that detached non-interacting binary members at the same evolutionary phase should have identical chemistry (Gizis & Reid 1997; Martín et al. 2002). This was corroborated by studies such as Hawkins et al. (2020) and Andrews et al. (2018) in the optical, and Lim et al. (2024) and Andrews et al. (2019) in the near-IR, who showed that wide binary pairs at similar evolutionary stages were chemically homogeneous to between 0.02–0.1 dex.

As the separation between members decreases to tens of AU or even less, the chances of interactions increase. Binaries in this regime—considered “close binaries”—are objects of great interest to understanding stellar evolution and chemical enrichment. Mass transfer events can impact the surface abundances of elements like carbon and s-process neutron capture elements (e.g., Barium), which are synthesised in stars on the asymptotic giant branch (AGB), before being dispersed into the interstellar medium through thermal pulses (Lugaro et al. 2003; Cseh et al. 2018). Common examples of post-interaction binaries are blue or yellow stragglers (Sandage 1953; Sun et al. 2021) and barium stars (Bidelman & Keenan 1951; Van der Swaelmen et al. 2017; Jorissen et al. 2019). Stars at such small separations can also undergo common envelope evolution, or be found in semi-detached configurations that cause large gradients in temperature and surface gravity. While there is nuance in the label “close binary”, within this paper we only mean single-lined spectroscopic binaries (SB1s), and its conclusions should not be generalized to other types of binary.

However, to our knowledge, no study has directly measured intra-pair chemical homogeneity in close binaries. This arises because resolving both members’ spectra at the separations of tens of AU or less is exceptionally challenging. Cases where both objects are similarly luminous result in unresolved spectroscopic binaries (SB2s), where it remains difficult to separate individual contributions from a single spectrum. In other cases, one companion is less luminous and is only detectable through the radial velocity variations (SB1s), or potentially eclipses, it induces in the brighter member (Stebbins 1911; Moe et al. 2019). In either case, detailed elemental abundances are challenging to derive for both members. However, constraining the chemistry of binaries at these close separations is crucial.

Studying close binaries in open clusters provides an opportunity to circumvent the limitations of SB2s. Stars in an open cluster form from a homogeneous distribution of gas at the same time, implying that they all have the same age, the same distance (Lada & Lada 2003), and most importantly the same birth abundances. Many studies support this assumption of OC chemical homogeneity (De Silva et al. 2007; Bovy 2016; Ness et al. 2018; Cheng et al. 2021; Sinha et al. 2024), constraining it within 0.1 dex across the light elements. There are evolutionary effects, such as atomic diffusion, and potential pollution events, such as rocky planet ingestion, that have been shown to cause chemical inhomogeneities. However, these events are either located in predictable parts of evolutionary space or are very short-lived (Souto et al. 2019; Michaud et al. 2015; Mack et al. 2016; Vejar et al. 2021).

Since close binaries that form in open clusters are also subject to the principle of identical birth chemistry, it is possible to measure the effect of close binarity and stellar interactions without measuring the abundances of both binary members. Indeed, previous works such as Ramos et al. (2024) have studied the overall abundances of spectroscopic binaries in clusters. We intend to take this concept further, to compare the chemical abundances of a cluster SB1 primary against that of a nonbinary cluster sibling star at the same evolutionary phase in order to directly measure the chemical similarity between cluster SB1s and single stars.

This work aims to constrain the chemical homogeneity of SB1s, compared to single stars, in open clusters within a large set of abundances. The structure of the paper is as follows: Section 2 outlines the survey data, determination of open cluster membership, and characterisation of binarity. Section 3 discusses the calculation of orbital parameters for binaries as well as the derivation of abundances. Section 5 presents the results of our work, and Section 6 compares our results to previous findings.

2 OPEN CLUSTER SAMPLE SELECTION

2.1 SDSS-V

The spectra and radial velocities we use are drawn from the Milky Way Mapper (MWM; J.A. Johnson, *in prep*), a component of the fifth generation of the Sloan Digital Sky Survey (SDSS, Kollmeier et al. 2025, 2017). We use data from Data Release 19 (DR19; SDSS Collaboration et al. 2025), which builds off of the observing strategies and survey goals outlined in SDSS Data Release 18 (Almeida et al. 2023) and includes observations of over one million targets cumulatively observed between SDSS-III and -V (Eisenstein et al. 2011; Blanton et al. 2017; Abdurro’uf et al. 2022).

SDSS-V/MWM uses two 2.5 m telescopes: the Sloan Foundation Telescope at APO (Gunn et al. 2006) and the du Pont Telescope at LCO (Bowen & Vaughan 1973). Both are outfitted with nearly identical custom-built 300-fibre APOGEE spectrographs (Wilson et al. 2019), with a resolution of $R \sim 22,500$, spanning the range of wavelengths between 1.51–1.70 μm . Unlike SDSS-IV, which used a plug-plate system, SDSS-V now uses robotic fibre positioners (Pogge et al. 2020), which benefited from the adoption of a three-element corrector for the Sloan telescope at APO (Barkhouser et al. 2022).

We use stellar metadata, radial velocities, and fundamental stellar parameters from the DR19 `mwmAllStar`, `mwmVisit`, and `astraAllStar` tables¹. We use spectra from the DR19 `mwmStar` files, which contain reduced, radial velocity corrected, resampled, and pseudo-continuum-normalized data. We also make use of the ASPCAP DR19 linelist, which is described in Smith et al. (2021), for our final line selection as detailed in Section 4.2.

2.2 Stellar Quality Cuts

Our goal is to define a sample of open cluster member stars for which we can (i) confidently infer a likelihood of having a close binary companion and (ii) measure reliable elemental abundances. To that end, we apply a series of quality cuts to the stellar spectra at the visit and combined level and to the initial stellar properties inferred from those spectra.

Following the recommendations in Price-Whelan et al. (2020), we

¹ <https://www.sdss.org/dr19/mwm/astra/output-files/>

enforce the following visit-level quality cuts in the `spectrum` flag column² at the `mwmVisit` level:

```

BITMASK 3; VERY_BRIGHT_NEIGHBOR == False; Star has neighbor more than 100 times brighter.
BITMASK 9; PERSIST_HIGH == False; Spectrum has at least 20 percent of pixels in high persistence region.
BITMASK 12; PERSIST_JUMP_POS == False; Spectrum has obvious positive jump in blue chip.
BITMASK 13; PERSIST_JUMP_NEG == False; Spectrum has obvious negative jump in blue chip.
BITMASK 16; SUSPECT_RV_COMBINATION == False; RVs from synthetic template differ significantly (~2 km/s) from those from combined template.
    
```

We enforce the following quality cuts in the `spectrum` flag column at the `mwmAllStar` level:

```

BITMASK 2; BRIGHT_NEIGHBOR == False; Star has neighbor more than 10 times brighter.
BITMASK 3; VERY_BRIGHT_NEIGHBOR == False; Star has neighbor more than 100 times brighter.
BITMASK 16; SUSPECT_RV_COMBINATION == False; RVs from synthetic template differ significantly (~2 km/s) from those from combined template.
    
```

and in the `results` flag column at the `mwmAllStar` level:

```

BITMASK 6; TEFF_GRID_EDGE_BAD == False; Teff is within 1/8th of a step from the grid edge
BITMASK 8; LOGG_GRID_EDGE_BAD == False; logg is within 1/8th of a step from the grid edge
BITMASK 10; V_MICRO_GRID_EDGE_BAD == False; v_micro is within 1/8th of a step from the grid edge
BITMASK 14; M_H_ATM_GRID_EDGE_BAD == False; [M/H] is within 1/8th of a step from the grid edge
    
```

For this study, we limit our analysis to FGK stars within the range of $4000 < T_{\text{eff}} < 6500$ K. To mitigate the risk of contamination from radial velocity jitter, a phenomenon found in upper giant stars (Shroyer & Carlberg 2020), we also remove any stars with $\log g < 1$. We set a limit of $\text{SNR} > 100$ to ensure we can recover blended Ce II lines. We calculate the number of visits by summing the number of `mwmVisit` entries that pass the quality cuts outlined above. We also remove any stars identified as SB2s from Kounkel et al. (2021), as studies of double-lined spectroscopic binaries require specialised analysis that is beyond the scope of this project.

To ensure the time-series RVs are sufficiently reliable for both the binarity and cluster membership determinations, we enforce that:

```

e_v_rad < 1 km s-1. Applied at the mwmVisit and astraStarASPCAP levels. This cut is made to exclude spurious, poorly-constrained, RV measurements
log g ≥ 1.0, to mitigate risk of contamination from RV jitter. Applied at the astraStarASPCAP level.
n_visits ≥ 5 Applied at the astraStarASPCAP level.
    
```

While it is possible to identify binaries using only 3 RV visits, this is insufficient to constrain parameters such as orbital separation (Castro-Tapia et al. 2024; Badenes et al. 2018). Therefore we opt to only include stars with $N \geq 5$ visits such that constraints on orbital parameters is plausible.

Finally, to ensure that we are analysing stars for which we can reliably determine chemical abundances using our existing tools (Section 4.2), we use the entries in `astraStarASPCAP` to require that there are no failures in the global $[M/H]$ or $[\alpha/M]$:

```

m_h_atm_flag == 0
alpha_m_atm_flag == 0
    
```

2.3 Open Cluster Membership

We start with the Cantat-Gaudin et al. (2020) open cluster catalogue, which includes membership probabilities, ages, and distances for approximately 2000 open clusters based on five inputs (α , β , μ_{α^*} , μ_{β^*} , and ϖ) from Gaia DR2. We tested using the Gaia DR3-based catalogue from Hunt & Reffert (2023) but found it did not expand our sample size. Furthermore, the systematically younger ages in this catalogue compared to other literature values (see, e.g., Section 3 of Otto et al. 2026) could lead to systematically biased atmospheric parameters (Section 4.1).

We match the `astraStarASPCAP` sample defined in Section 2.2 to all Cantat-Gaudin et al. (2020) stars with membership probability $P \geq 0.7$ and a position within three cluster radii, defined in Cantat-Gaudin et al. (2020) as the radius which contains 50% of members, from the cluster centre.

Within these crossmatched clusters, we ensure minimal field star contamination by iteratively rejecting stars further than two standard deviations from the cluster median in the following four parameters: radial-velocity (RV), δ_{α^*} , δ_{β^*} , and ϖ . Here, the two proper motion parameters and parallax are drawn from Gaia DR3, but radial velocities are drawn from APOGEE spectra.

After our quality cuts and cluster membership selection, we are left with 267 stars in 20 open clusters.

3 BINARITY AND BINARY PROPERTIES

The methods described in this binary selection are all sensitive to different areas of parameter space, and thus differing classifications of binarity between metrics are to be expected. Due to the 10-year observational baseline of SDSS, we are ideally suited to observe SB1s with periods ≤ 4000 days. In particular, both the `JOKER` and `ULTRANEST` can leverage this footprint to confidently constrain parameters for edge-on binaries. However, as inclination ($\sin(i)$) increases, the induced RV-variation decreases, reducing these tools' ability to detect binarity in a way that Gaia RUWE is independent of. Therefore, we categorise a star as binary if any one of the above methods classifies it as such. While APOGEE RVs are not sensitive to binaries with periods longer than 4000 days, binaries in this regime are beyond separations at which they can interact.

Finally, the expected binary fraction in FGK stars at solar metallicity ($[M/H] > -0.5$) is $\sim 10\%$, though studies of open clusters measure higher spectroscopic binary fractions ($\sim 30\%$) (Moe et al. 2019; Geller et al. 2021). Between this binary fraction and our detection sensitivity, it is unlikely that any contaminants in our baseline non-binary sample could skew our results.

3.1 RV Scatter

We measure ΔRV_{max} , defined as $RV_{\text{max}} - RV_{\text{min}}$, for each star in our sample, using the `mwmVisit` radial velocities. Following the recommendations of Badenes et al. (2018), we classify stars with $\Delta RV_{\text{max}} > 3 \text{ km s}^{-1}$ as likely binaries, and stars with $\Delta RV_{\text{max}} < 3 \text{ km s}^{-1}$ as potential nonbinaries.

² More detailed documentation on the flagging schema and quality cuts can be found here: <https://www.sdss.org/dr19/tutorials/>

3.2 The Joker Orbital Estimates

The JOKER is a custom Monte Carlo sampler that uses variability in radial velocity visits to derive posterior solutions in six parameters: period, eccentricity, argument of pericentre, phase, velocity amplitude, and barycentre velocity. To accomplish this, it densely samples from a set of prior distributions in these six parameters that spans the entire parameter space and performs a brute force rejection sampling. While this approach has the advantage of avoiding local minima for which traditional MCMC methods are at risk, it requires a significant upfront investment. Specifically, prior samples must densely sample the entire parameter space. To ensure sufficiently dense prior sampling, we follow the recommendation of Price-Whelan et al. (2020) and generate 100,000,000 prior samples. However, in cases where rejection-sampling determines the posterior solution is unimodal, the JOKER provides MCMC sampling routines to determine orbital solutions.

We make modifications to the default JOKER initialiser to tune it for open cluster studies. In particular, we adopt a normal distribution in barycentric velocity, centred at the median cluster radial velocity ($\langle RV_{\text{cluster}} \rangle$), with a standard deviation equal to the cluster velocity dispersion ($\sigma(RV_{\text{cluster}})$); these values are calculated using the median radial velocities for cluster members published in the DR19 astraStarASPCAP file. This choice is driven by the fact that open cluster binaries, being gravitationally bound to the cluster, should have a systemic velocity similar to that of an unpaired star in the same cluster. The prior samples are drawn from the following distributions³:

$$\text{Period } (P) = \log(\mathcal{U}(2, 4000))$$

$$\text{eccentricity } (e) = \text{Beta}(0.867, 3.03)$$

$$\text{Mean anomaly } (M_0) = \mathcal{U}(0, 2\pi)$$

$$\text{Pericenter argument } (\omega) = \mathcal{U}(0, 2\pi)$$

$$\text{RV jitted } (s) = \mathcal{N}(\mu_y, \sigma_y^2)$$

$$\text{RV amplitude } (K) = \mathcal{N}(0, \sigma_K^2),$$

$$\text{Systemic velocity } (v_0) = \mathcal{N}(v_{\langle RV_{\text{cluster}} \rangle}, v_{\sigma(RV_{\text{cluster}})})$$

Where period P is in days; M_0 and ω are in radians; and s , K , and v_0 are in km s^{-1} . See the JOKER documentation⁴ for more information.

We also correct for any potential RV uncertainty underestimation with Equation 1 from Price-Whelan et al. (2020):

$$\sigma_{\text{RV, total}}^2 = (3.5(\sigma_{\text{RV}})^{1.2})^2 + (0.072)^2 \text{ km s}^{-1} \quad (1)$$

to ensure that the visit-level velocity uncertainties are conservatively estimated.

We create a baseline for each star by generating synthetic radial velocity visits drawn from a normal distribution, with the centre at the observed v_0 , and dispersion equal to the observed star's radial velocity uncertainty. Both synthetic and observed data are passed to the JOKER which determines the log-likelihood of an orbital solution. We then compare the log-likelihoods of the best fit solutions, where

$$\mathcal{L}_{\text{observed}} - \mathcal{L}_{\text{synthetic}} > 4.6 \quad (2)$$

indicates that the observed data are likely from a binary star. This threshold was inherited from Price-Whelan et al. (2020), but we tested different thresholds and found no difference in our final results.

³ Here \mathcal{U} refers to a uniform distribution and \mathcal{N} refers to a normal distribution.

⁴ <https://thejoker.readthedocs.io/en/latest/examples/1-Getting-started.html>

In the vast majority of cases, stars that are identified as binaries have highly multimodal posteriors. As a result, no single confident orbital solution can be recovered from them.

However, in some cases, the posterior sampling is unimodal, and we can converge on a single orbital solution. This typically occurs when the star has sufficient radial velocity visits throughout the entirety of its orbital period. Typically, these stars have $N_{\text{visits}} \geq 7$, but we note that many stars with $N_{\text{visits}} \geq 7$ do not have unimodal posteriors due to sparse sampling across the entire orbital period.

3.3 UltraNest Orbital Estimates

For stars with $N \geq 7$ visits, we corroborate our JOKER orbital solutions using a nested sampling method as implemented in Müller-Horn et al. (2025b). While this approach has many similarities to the JOKER, it is built on a nested sampler called ULTRANEST⁵ instead of a classic MCMC. As such, it is less prone to being trapped in local minima when sampling the parameter space, which gives it a distinct advantage when constraining potentially multimodal solutions. It also does not require generating a computationally expensive prior cache like the JOKER. The prior distributions used are:

$$e = \mathcal{U}(0, 1)$$

$$P = \mathcal{U}(0.2, 4000)$$

$$M_0 = \mathcal{U}(0, 2\pi)$$

$$\omega = \mathcal{U}(0, 2\pi)$$

$$\tau = \mathcal{U}(0, 1)$$

$$K = \mathcal{U}(0, 200),$$

$$v_0 = \mathcal{N}(0, 100)$$

Here τ is the orbital phase. We apply the same likelihood criteria derived for the JOKER here and inspect each orbital solution by eye to ensure it is a good fit to the observed data. From the sample of stars with $N \geq 7$ radial velocity visits, we determine confident unimodal orbital solutions for 16 of them, hereafter called ULTRANEST values (for consistency with Müller-Horn et al. 2025b). These 16 binaries will be used to analyse the relationship between abundance and orbital separation, while our multi-modal binaries will be used to study binary abundances at the population level.

We provide examples of our orbital fits for unimodal stars in Figure 1, and we compare the orbital solutions from the JOKER and ULTRANEST in Figure 2. Out of the 16 binaries we find that are confidently unimodal, all but one have consistent periods and eccentricities between the two codes. We also show the distribution of stars in period-eccentricity space in Figure 2. To further verify our orbital solutions, we cross-match our sample with the WIYN Open Cluster Study (WOCS; Mathieu 2000), which has conducted detailed photometric, astrometric, and spectroscopic studies of open clusters, focusing on open cluster binaries.

When cross-matched to our sample, we find that only four stars from the WOCS survey are included, all of which are members of M67 and were analysed in Geller et al. (2021). Within these stars, we compare the derived periods and eccentricities as shown in Figure 2. From this, we see that the ULTRANEST and the JOKER orbital solutions are in good agreement with those derived by Geller et al. (2021). The JOKER appears to underestimate eccentricity, likely due to the use of a Beta distribution prior, which favours low eccentricities, instead of a Uniform distribution like ULTRANEST.

⁵ <https://johannesbuchner.github.io/UltraNest/index.html>

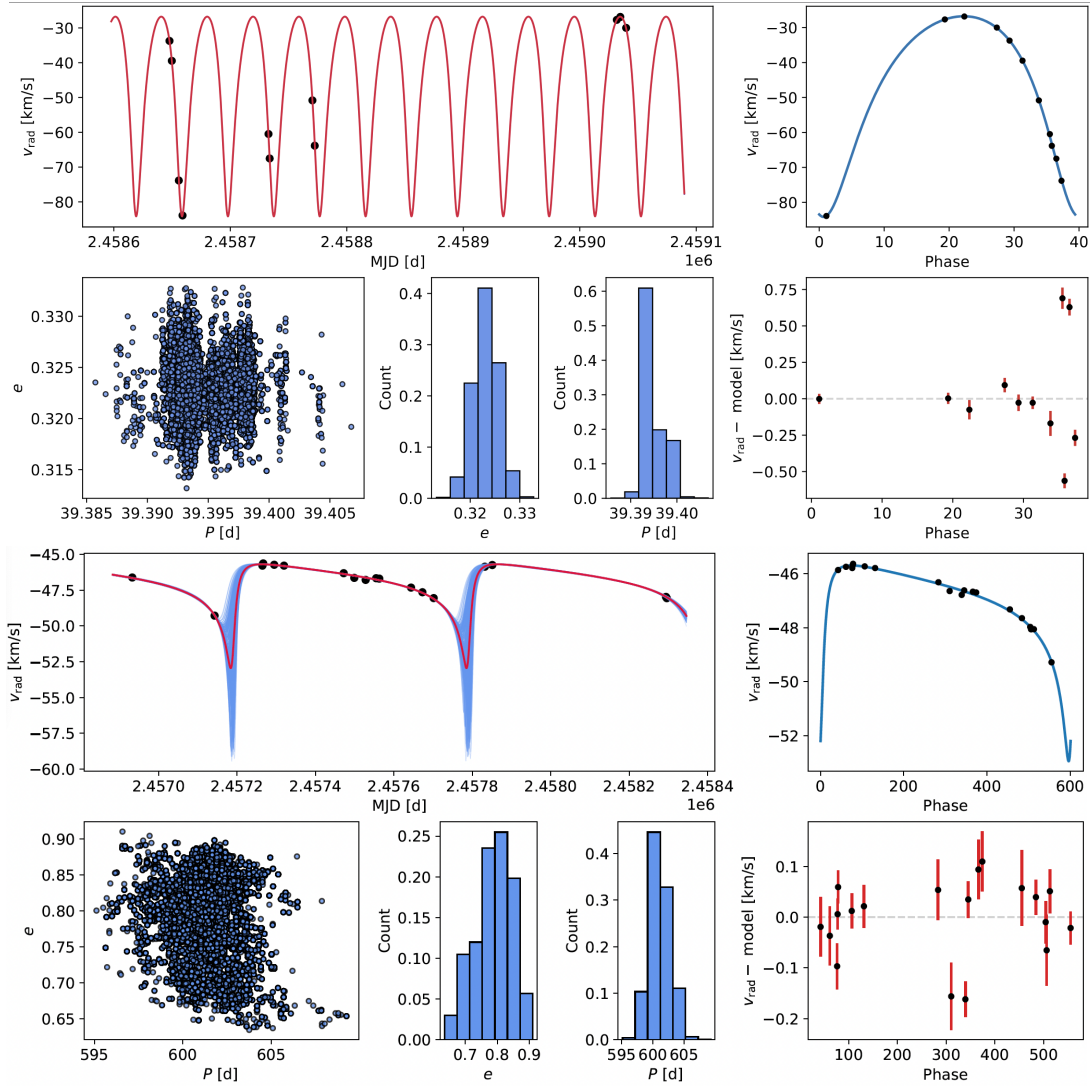


Figure 1. *Top:* The orbital fit for SDSS 66658896, a short-period binary, as determined by ULTRANEST. We show the best fit orbital solution compared to the observed data points in the top left in MJD and orbital phase across the top row. In the bottom row, we show the ULTRANEST final live-point sampling for the orbital period, histograms of the sampling counts for period and eccentricity, and the residual between the observed data and model across orbital phase. *Bottom:* The orbital fit for SDSS 66661885, a long-period binary, as determined by ULTRANEST. The ordering of information in panels is the same as in the top plot.

3.4 Gaia RUWE & NSS

We supplement our sample with Renormalised Unit Weight Error (RUWE) measurements from Gaia DR3, which measures excess scatter in astrometric position as a potential proxy for binarity (Gaia Collaboration et al. 2023a; Müller-Horn et al. 2025a). Using the GAIAUNLIMITED package (Castro-Ginard et al. 2024), we calculate individual RUWE thresholds for each star, which range between 1.19 and 1.3. Stars with measured RUWE greater than their GAIAUNLIMITED threshold estimate are classified as probable binaries. We choose this method over a flat threshold of 1.4 as Castro-Ginard et al. (2024) demonstrate that such a restrictive threshold leaves many binaries classified as single stars. Of the 28 stars identified as binaries by their Gaia RUWE, seven were already identified as a binary by our JOKER/ULTRANEST analysis.

Finally, we cross-reference with the Gaia Non-Single-Star (NSS) catalogue (Gaia Collaboration et al. 2023b) to check for any orbital solutions. Only two stars in our sample, Gaia 604917728138508160

and 573967403529044352, have matches in the NSS catalogue, and both were detected as SB1s by our JOKER/ULTRANEST analysis.

We require that each cluster has at least one binary and one non-binary star. After removing clusters that do not pass this threshold, we are left with 222 stars (119 nonbinaries and 103 binaries) across 14 open clusters. A detailed cluster-by-cluster breakdown of our sample can be seen in Table 1. We note that due to the underlying survey selection criteria, exhaustive quality cuts, and restrictive requirements on classification as nonbinary or binary, these are not reflective of the true underlying cluster binary fractions and should not be used as such.

4 ABUNDANCE DETERMINATION

4.1 Atmospheric Parameters

While large industrial pipelines such as ASPCAP and Astra are well suited for chemical species with clean absorption features—such as

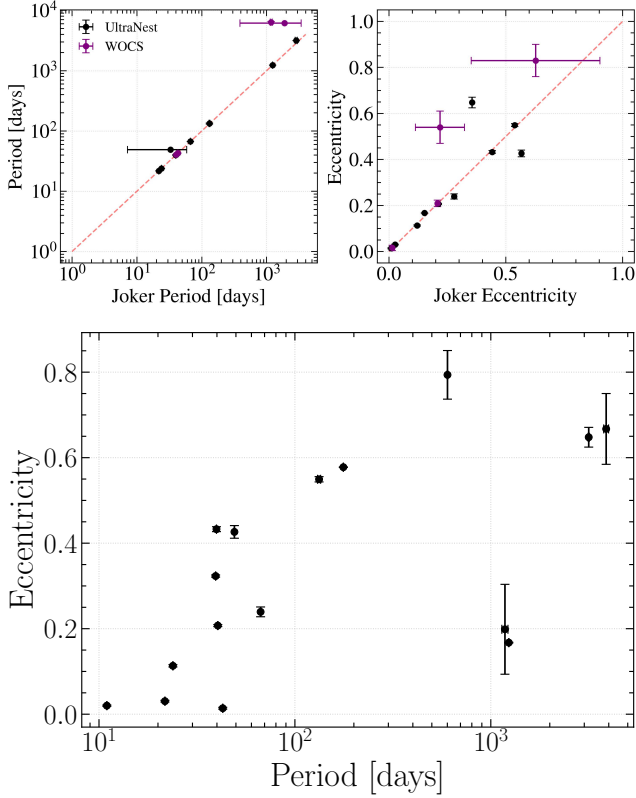


Figure 2. *Top:* A comparison between the orbital solutions for unimodal stars analysed by the JOKER, ULTRANEST, and WOCS. It is clear that while both codes exhibit reasonable agreement in period, there is significantly less agreement in eccentricity. This is likely due to the different priors used in the two codes. It is also clear that the JOKER/ULTRANEST parameters broadly agree with those derived independently by WOCS. *Bottom:* The period-eccentricity distribution of all binaries in our sample with confident orbital solutions, as solved for by ULTRANEST.

Table 1. A breakdown of the binary and nonbinary populations in each cluster used in this study. We also provide the ages, distance moduli, and A_V —drawn from Cantat-Gaudin et al. (2020)—used to analyse members of each cluster.

Cluster	$\log(\text{Age}/\text{yr})$	D_{mod}	A_V	Nonbinaries	Binaries
Collinder 69	7.10	8.10	0.25	2	1
Melotte 111	8.81	4.67	0.00	2	5
Melotte 20	7.71	6.17	0.30	10	7
Melotte 22	7.89	5.55	0.18	6	2
NGC 188	9.85	11.15	0.21	5	6
NGC 2158	9.19	13.17	1.44	4	3
NGC 2168	8.17	9.79	0.46	12	16
NGC 2243	9.64	12.85	0.02	4	3
NGC 2420	9.24	12.06	0.04	9	4
NGC 2632	8.83	6.31	0.00	7	4
Messier 67	9.63	9.75	0.07	30	46
NGC 6791	9.80	13.13	0.70	10	10
NGC 6819	9.35	12.21	0.40	13	9
NGC 752	9.07	8.42	0.07	10	6

Fe, Mg, and Si—they are significantly less equipped to deal with weak or blended features such as those from Ce and Nd (Hayes et al. 2022; Cunha et al. 2017; Hasselquist et al. 2016). As these are s -process elements that can identify post-mass transfer objects, accurate determination of them is crucial for this analysis. Therefore we opt to derive our own abundances. To ensure a homogeneous analysis, we derive chemical abundances for every chemical species in our study. This also has the added benefit of allowing us to be judicious with our line selection, and exclude many poorly fit absorption lines or temperature-sensitive features.

In this section we leverage the precise distances and ages from Cantat-Gaudin et al. (2020), MIST isochrones, and SDSS-V effective temperatures to derive stellar masses, and empirical atmospheric parameters such as surface gravity and microturbulent velocity.

We make use of the distance moduli (DMNN), extinctions (AVNN), and ages (AgeNN) from Cantat-Gaudin et al. (2020) for each cluster. To determine the metallicity of each cluster, we use the median $[\text{Fe}/\text{H}]$ abundance derived by Astra. We then interpolate a MIST isochrone to those values for each cluster using the ISOCHRONES package (Paxton et al. 2011; Morton 2015; Dotter 2016; Choi et al. 2016). Observed stars in our sample are matched to corresponding interpolated isochrone Equivalent Evolutionary Points (EEPs) by performing a chi-squared minimization in Gaia ($BP - RP$) and G magnitudes. We also test matching on the 2MASS (Skrutskie et al. 2006) J , H , and K_s filters and find that this does not meaningfully change the derived parameters.

The APOGEE wavelength range includes many temperature-sensitive lines (Mészáros et al. 2025), and the effective temperatures from Astra are broadly trustworthy, the methodology for which is described in García Pérez et al. (2016). To verify this, we independently derive effective temperatures for a subset of stars in our sample using their *ugrizJHK* photometry with the InfraRed Flux Method (IRFM; e.g., Casagrande et al. 2010). We follow a similar methodology to Hawkins et al. (2016), and find strong agreement between the two sets of temperatures ($\Delta T_{\text{eff}} < 150 \text{ K}$). As we find stronger agreement between IRFM and the uncalibrated temperature (`raw_teff`) values, we use them instead of the calibrated effective temperatures.

Unlike effective temperature, the APOGEE region does not have as many surface-gravity dependent lines (Mészáros et al. 2025). Therefore, it uses multiple calibration methods, such as comparison to asteroseismic $\log(g)$ values, to derive calibrated surface gravities (see Casey et al. in prep). However, these calibrations do not extend to stars with $T_{\text{eff}} < 4500 \text{ K}$ due to the lack of asteroseismic calibrations in that part of parameter space. Since many of our stars fall below this limit, rederiving correct surface gravities is imperative for our abundance analysis. To derive surface gravities, we use the Stefan–Boltzmann relation:

$$\log(g)_{\star, \text{empirical}} = \log(g_{\odot}) + \log\left(\frac{M_{\star}}{M_{\odot}}\right) + 4\log\left(\frac{T_{\star}}{T_{\odot}}\right) + 0.4(M_{\text{bol},\star} - M_{\text{bol},\odot}). \quad (3)$$

Here M_{\star} and $M_{\text{bol},\star}$ are drawn from the star’s interpolated EEP, and T_{\star} is the star’s `raw_teff` value. We use the following solar values: $\log(g)_{\odot} = 4.438 \text{ dex}$, $M_{\text{bol},\odot} = 4.75$, and $T_{\text{eff},\odot} = 5772 \text{ K}$. These are the same values recommended by Prša et al. (2016) and are derived from estimates of the solar photospheric radius, radiative luminosity, and measurements of nominal total solar irradiance. We also use these within our abundance analysis to ensure consistency. While stars on the giant branch and red clump have relatively consistent Astra and isochrone-derived values, there are significantly more

offsets within the dwarf stars, particularly at lower temperatures, as shown in Figure 3. We find that the Astra-derived surface gravities are systematically overestimated for stars below the giant branch, and that for stars near the turn-off, the $\tau_{\text{raw_teff}}$ values are far better aligned with isochrone predictions.

From our empirically derived surface gravity, we determine the microturbulence using the equation from Masseron et al. (2019), where μ_t is in km/s:

$$\mu_t = 2.488 - 0.866 \log(g) + 0.1567 (\log(g))^2. \quad (4)$$

Finally, we measure the $v \sin i$ for all the stars in our sample using KORG (Wheeler et al. 2023), as Astra only measures $v \sin i$ for dwarf stars. As the resolution of APOGEE spectra is not sensitive to $v \sin i \leq 5 \text{ km s}^{-1}$, and most giant stars are slow rotators, $v \sin i$ is not measured for them. This is due to the fact that giant stars are generally slow rotators ($v \sin i \leq 5 \text{ km s}^{-1}$) due to magnetized winds from the convective envelope carrying away angular momentum (de Medeiros et al. 1996; Tayar et al. 2015). However rapid-rotation on the red giant branch (RGB) can be seen as an indicator of unusual history, such through planetary ingestion or binary interaction (Carlberg et al. 2012; Patton et al. 2024). However, to identify potential stars of interest in our sample, we do want to constrain $v \sin i$ as much as we can.

Using the effective temperatures and now-determined surface gravities, as well as the star’s [Fe/H], [Mg/H], and [Si/H] abundance from BACCHUS, we synthesize a set of synthetic spectra between $0 \leq v \sin i \leq 80 \text{ km s}^{-1}$, with a stepsize of 5 km s^{-1} . We then perform a chi-squared minimization across the entire spectrum and use a `CubicSpline`, from the `SciPy` package, to determine the best-fit $v \sin i$. For dwarf stars with Astra $v \sin i$, we compare them to our derived values and find strong agreement, as shown in Figure 4. We note that the difference between the Astra and our $v \sin i$ estimates increases at large values, but it is almost always less than $\Delta v \sin i \sim 5 \text{ km s}^{-1}$. We find strong agreement between the two samples at values below $\sim 30 \text{ km s}^{-1}$ ($\sim 94\%$ of the sample).

For the giant stars in our sample, we find that $\sim 85\%$ have $v \sin i \leq 5 \text{ km s}^{-1}$. We only find one giant star (Gaia 865402924795303040) that could be considered a rapid-rotator, with $v \sin i = 12.7 \pm 1.7 \text{ km s}^{-1}$, though it was not classified as a binary by our analysis.

4.2 Derivation of Chemical Abundances with BACCHUS

We use the Brussels Automatic Code for Characterizing High accuracy Spectra (BACCHUS; Masseron et al. 2016), an “on the fly” spectrum synthesis code, to derive elemental abundances from stacked `mwmStar` spectra. BACCHUS relies on the grid of MARCS model atmospheres (Gustafsson et al. 2008), Masseron’s model atmosphere thermodynamic structure interpolator, and the radiative transfer code `Turbospectrum` (Plez 2012). One of the primary benefits of BACCHUS over the Astra abundances is that it is better suited to determine abundances for weak or strongly blended lines, such as Ce and Nd. To model a stellar atmosphere, BACCHUS requires five parameters: T_{eff} , $\log(g)$, μ_t , [M/H], and convolution. Given the lack of usable Fe II lines within the APOGEE wavelength range required for a traditional excitation-ionization balance, we forego the derivation of temperature and surface gravity within BACCHUS. Instead, we fix each star’s T_{eff} , $\log(g)$, and μ_t at the values derived in the previous section. We set the initial guess for [M/H] at the same median cluster [Fe/H] used to interpolate its isochrone. We then solve for each star’s individual metallicity using Fe I.

Unlike other spectral synthesis codes like MOOG (Snedden 1973) or KORG, BACCHUS does not measure $v \sin i$; instead, it uses a single convolution parameter that acts as a catch-all for rotation and instrumental broadening. To solve for this parameter, we follow a similar methodology to Hayes et al. (2022) and use three Si I lines: 16680.8Å, 16828.2Å, and 16094.8Å, as shown in Figure 3. We choose Si I as the lines are strong and clean, but we also experiment with OH and Ti I lines. We find that there is no significant difference in the derived convolutions. Finally, due to carbon’s impact on model atmospheres, especially in cooler stars where molecules are present (e.g., CO and CN), we solve for the carbon abundance of each star to establish a proper chemical equilibrium.

Once all five parameters and C have been established, we derive abundances for the following chemical species: Si, Fe, C, N, O, Na, Mg, Al, Ca, Ti, Cr, Ni, Ce, and Nd. While we initially measure abundances for all the observed absorption features measured in the APOGEE DR19 linelist, our final results only include information from a select set of confident lines, discussed in Section 4.2.1. We iterate this entire analysis twice for each star to ensure self-consistency in the atmospheric parameter and abundance determination. We run BACCHUS in “manual” mode, using the packages `BACCHUS_TOOLS`⁶ and `PyBACCHUS`⁷ to interface with BACCHUS from within Python. Finally, we solar-scale our abundances using Grevesse et al. (2007) recommended values.

Our final abundances for each star are taken as the median of all lines flagged as good by the `chi2` method⁸. We also only select lines where the difference in line abundance derived through `chi2` and `eqw` is less than 0.3 dex. Finally, for species with more than two lines, we remove any individual line with abundance measurements more than 3σ from the median. Because every chemical species depends on a correctly estimated microturbulence and convolution, we limit our sample to stars with confidently measured Si and Fe abundances. For these two elements, we require all four abundance determinations to have `flag = 1` for a line to be used. Our derived model atmospheres closely agree with the observed spectra, as shown in Figure 5.

4.2.1 Line Selection & Temperature Trends

To ensure that we have no trends in temperature that could affect our results, we measure the T_{eff} vs. $A(X)$ relation for every elemental line in the APOGEE wavelength range, using M67 and Melotte 22 (the Pleiades). We choose the Melotte 22 as it allows us to compare with the line selection done by Grilo et al. (2024). Furthermore, these two clusters provide excellent coverage across the entire HR diagram, with robust coverage on the main sequence.

We quantify each temperature-line abundance relationship using `SciPy`’s `linregress` function. We remove any lines with significant systematic offsets ($\Delta A(x) \geq 0.2 \text{ dex}$), or trends in temperature, which we classify as a slope greater than $4 \times 10^{-5} \text{ dex K}^{-1}$. Lines with slopes greater than this limit would induce 0.1 dex of chemical scatter (if they were the only lines being used) across the temperature range spanned by our sample. We also remove lines with $R^2 < 0.5$ as this implies the line has a large star-to-star scatter. Our final line selection can be found in Table 2.

⁶ https://github.com/catherine-manea/BACCHUS_Tools

⁷ <https://github.com/rocketxturtle/PyBACCHUS>

⁸ For a more detailed discussion of the strengths and weaknesses of BACCHUS’s abundance determination methods, as well as its flagging metrics, please see Section 3.0 in Hayes et al. (2022).

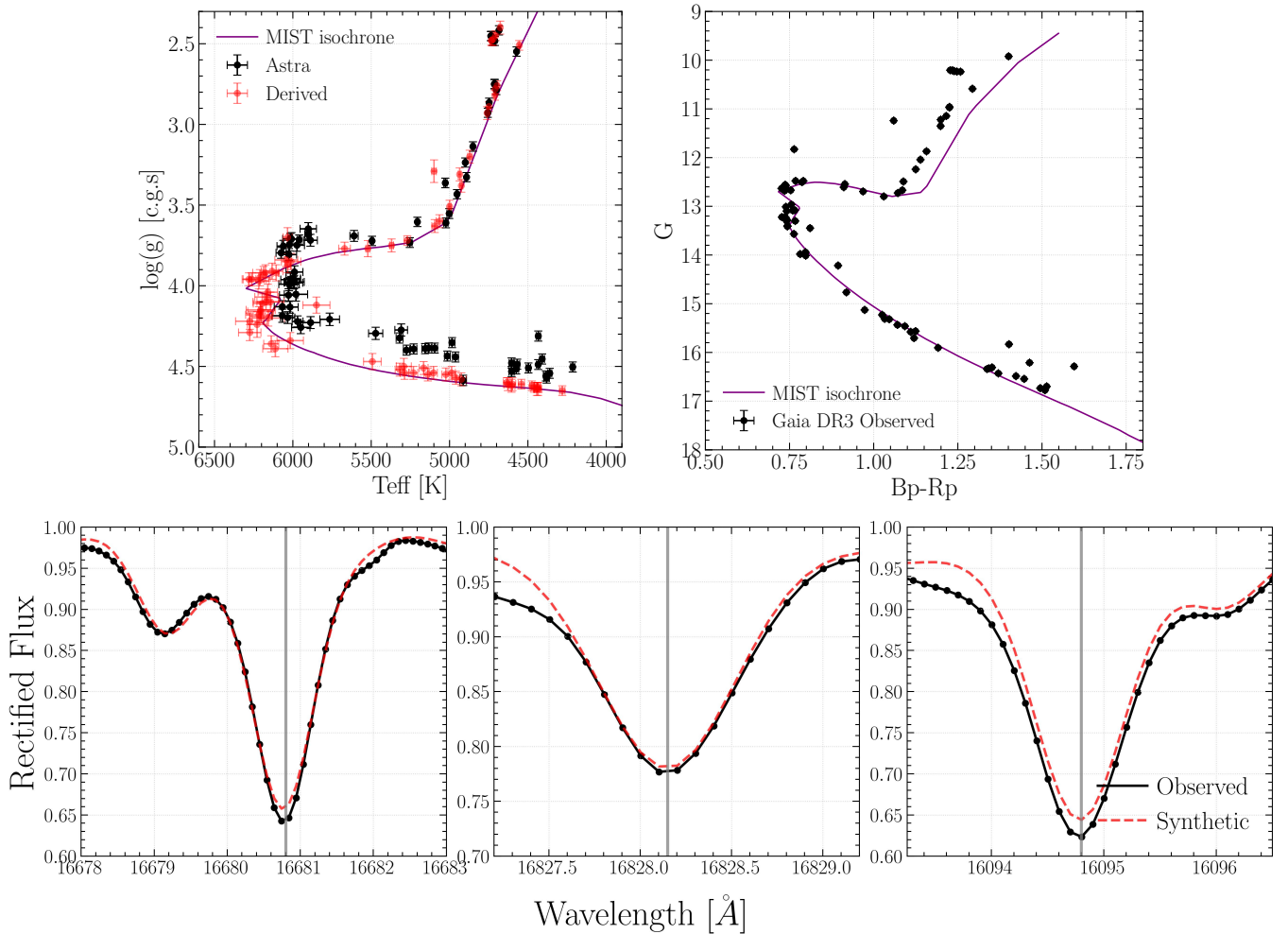


Figure 3. *Top Left:* A comparison of the interpolated MIST isochrone for Messier 67 (NGC 2682) and the observed stars in $(BP - RP)$ and G . *Top Right:* Here we show the effective temperatures and surface gravities used, as compared to the published values, for M67. *Bottom:* We show the three Si lines used in this study to derive broadening: 16680.8 \AA , 16828.2 \AA , and 16094.8 \AA , with the observed spectrum of a typical star in black. We show a synthetic spectrum generated using an interpolated MARCS stellar atmosphere at that star’s derived $\log(g)$, T_{eff} , $[\text{Fe}/\text{H}]$, and microturbulence in red. While there are slight differences between the observed and synthetic spectrum on the left wing in the rightmost plot, this does not affect the synthetic fit to the line core—and therefore the derived convolution.

4.2.2 Abundance Uncertainties

BACCHUS does not propagate the uncertainties on the atmospheric parameters through the abundance determination. As a result, the abundance uncertainties it measures are strictly from the line-to-line dispersion. To ensure that the abundance uncertainties are correctly estimated, we create a grid in temperature, surface gravity, and $[\text{M}/\text{H}]$ that spans the entire parameter space of our sample, with steps of 200 K, 0.5 dex, and 0.2 dex, respectively. Given that we limit our sample to stars with $\text{SNR} > 100$, we assume there is no dependency on that parameter. We experimented with finer step sizes in these three dimensions and found no significant difference in uncertainties; therefore, these steps were chosen for the sake of computational efficiency. Within each bin, we arbitrarily choose ten stars and Monte-Carlo their temperatures, isochrone-derived surface gravities, and derived microturbulences within their uncertainties. Given that the derivation of $[\text{M}/\text{H}]$ and convolution is determined in part by these three parameters, this effectively Monte-Carlos all five stellar parameters. For bins with fewer than ten stars, stars were reused as independent Monte-Carlo instances.

From this, we repeat the abundance derivation methodology described above to get abundances for each star. Within each bin of temperature, surface gravity, and metallicity, we measure the $[\text{X}/\text{H}]$ dispersion to estimate an empirical abundance uncertainty for stars in our sample at that effective temperature, surface gravity, and metallicity.

The cluster membership, orbital and atmospheric parameters, and derived abundances from this study will be included in a machine-readable table. The columns of this table are shown in Table 3.

5 RESULTS

5.1 Population Abundance Comparison

Here we compare the individual abundances of stars in our binary sample to nonbinary stars within the same cluster. To remove the influence of stellar evolution and observational noise on any part of the analysis, we compare binary-nonbinary pairs with $\Delta T_{\text{eff}} \leq 250$ K and $\Delta \log g \leq 0.25$ dex. This is particularly important for $[\text{C}/\text{N}]$, which is mass dependent and therefore sensitive to large differences

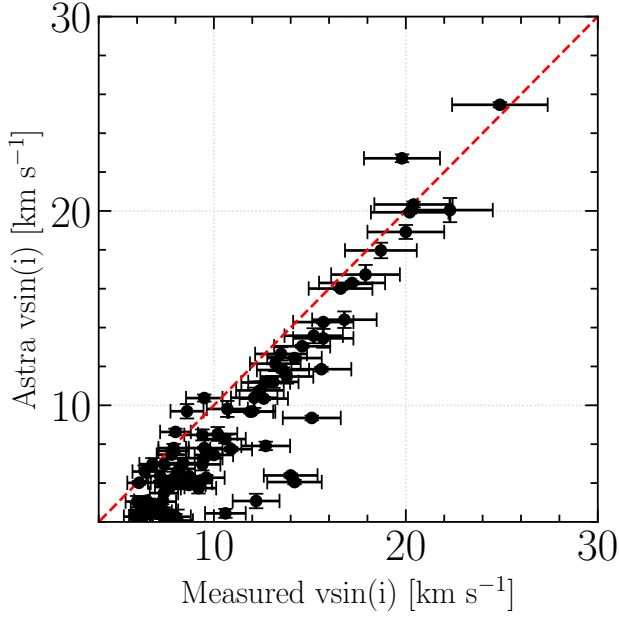


Figure 4. Here we compare the derived values of $v \sin i$ to the published Astra values. We find strong agreement between the two samples at values below $\sim 30 \text{ km s}^{-1}$ ($\sim 85\%$ of the sample).

Table 2. Atomic and molecular lines used for abundance determination. All wavelengths are given in air and in Angstroms (\AA).

Element	Solar Value	Wavelengths (\AA)
CO	8.39	15783.9, 16004.9, 16021.7, 16836.0, 16890.4
CN	7.78	15222.0, 15228.8, 15242.5, 15708.5
OH	8.66	15719.7, 16650.0
Na I	6.17	16373.9, 16388.9
Mg I	7.53	15879.5, 15886.2, 15954.5
Al I	6.37	16763.4, 16719.0
Si I	7.51	16680.8, 16828.2, 16094.8
Ca I	6.31	16136.8, 16157.4
Ti I	4.90	15715.6
Cr I	5.64	15680.1
Fe I	7.45	15207.5, 15662.0, 15686.3, 15774.1, 15904.4, 15911.3, 15920.7, 16006.8, 16042.7, 16125.9, 16180.9, 16207.7, 16213.5, 16225.6, 16522.1, 16541.6, 16645.9, 16665.5, 16753.0
Ni I	6.23	15605.6, 15632.6, 16584.4, 16585.4
Ce II	1.58	15784.8, 16376.5, 16595.2, 16722.5
Nd II	1.45	15368.1, 16053.6, 16262.0

in $T_{\text{eff}}/\log g$, even within a given cluster. Within each element, we measure the $\Delta[X/H]$, defined as the intra-pair difference in $[X/H]$ ($[X/H]_{\text{binary}} - [X/H]_{\text{nonbinary}}$), and compare it with the limits on open cluster homogeneity derived in [Sinha et al. \(2024\)](#). As a control, we compare the $\Delta[X/H]$ from our binary-nonbinary pairs to a set of $\Delta[X/H]$ measured with nonbinary-nonbinary pairs.

The results of this analysis can be seen in Figure 6. We find no systematic, universal enrichment or depletion in any of the elements we study – that is, the stars in the binary-nonbinary pairs are as similar to each other as the stars in the nonbinary-nonbinary pairs are. To corroborate this, we measure the similarity between the binary-nonbinary and nonbinary-nonbinary datasets using a two-sample Kolmogorov–Smirnov test. We measure $p > 0.5$ for all elements, implying that, as a population, the SB1 star abundances and single star abundances were drawn from the same underlying sample in a given cluster.

To ensure that the impact of abundance uncertainties is also considered in our analysis, we compute a binary-binary and nonbinary-nonbinary χ^2 value for each element, using Equation 3 from [Ness et al. \(2018\)](#). We find that the χ^2 distributions, also shown in Figure 6, for the binary-nonbinary and nonbinary-nonbinary samples are drawn from the same population across all the chemical species we measure. This implies that, as a population, close binarity has not had a statistical impact on the surface abundances of our SB1 stars.

5.2 Extended Analysis with GALAH

Due to the wavelength range of the APOGEE spectra, only Ce and Nd are available to trace s-process neutron capture abundances. While Ce is primarily an s-process element, Nd receives approximately 50% contribution from the r-process ([Prantzos et al. 2020](#)), making it less suitable to study potential post-mass-transfer objects. We supplement our results with abundance information from the Galactic Archaeology with HERMES (GALAH) Survey DR4 ([Buder et al. 2021, 2025](#)), which publishes abundances for 12 neutron capture elements: Rb, Sr, Y, Zr, Mo, Ba, La, Ce, Nd, Ru, Sm, and Eu. Given that Ba is an almost pure s-process element ([Lugaro et al. 2023](#)), it is the ideal tracer for identifying post-AGB mass-transfer objects. Using the GALAH DR4 `allstar` file, we apply the following quality cuts⁹ to ensure trustworthy abundance measurements:

```
snr_px_ccd3 > 30,
flag_sp == 0,
flag_fe_h == 0, and
flag_X_fe == 0,
```

where `flag_X_fe` includes the elements listed above.

When cross-matched to our MWM open cluster sample, we find only 38 common stars, all within M67 and NGC 2632. None of our unimodal binary stars appear in the GALAH cross-match. We repeat our analysis from Section 5.1, identifying pairs of binary-nonbinary and nonbinary-nonbinary stars with similar temperatures and surface gravities. We then measure the $\Delta[X/H]$ within the neutron-capture elements for these pairs.

Within our cross-matched GALAH sample, we find that none of the likely binaries are enhanced in the s-process neutron-capture elements as compared to their nonbinary counterparts, as shown in Figure 7. In particular, we find no evidence that any star is a post-AGB mass-transfer object, as the binary-nonbinary and nonbinary-nonbinary $\Delta[\text{Ba}/\text{H}]$ are consistent with one another. While it visually appears that Eu is potentially enhanced in binaries compared to nonbinaries, we note that this sample of Eu abundances is limited in size ($N = 9$) and strong conclusions cannot be drawn from it.

⁹ The quality cuts for SNR, stellar parameters, and $[\text{Fe}/\text{H}]$ are all drawn from <https://www.galah-survey.org/dr4/overview/>. The GALAH DR4 `allstar_240705.fits` file can also be found here.

Table 3. Summary Table of Parameters: List of columns in the stellar parameters table. [X/H] abundances are measured for the following elements: Fe, Si, C, N, O, Mg, Ca, Ni, Cr, Ti, Na, Al, Ce, and Nd. This table will be made available in machine readable format.

Column Name	Units	Description (\AA)
sdss_id		SDSS DR19 identifier
gaia_dr3_source_id		Gaia Data Release 3 identifier
RA	deg	Right ascension from Gaia DR3
DEC	deg	Declination from Gaia DR3
parallax	mas	Parallax from Gaia DR3
pmRA	mas yr ⁻¹	Right ascension proper motion from Gaia DR3
pmDEC	mas yr ⁻¹	Declination proper motion from Gaia DR3
X_mag		Apparent magnitude in the $B_p R_p G, JHK, W1W2, ugriz, y$ filters
snr		Signal-to-noise of the stacked mwmStar spectrum used.
v_rad	km s ⁻¹	Median radial-velocity across all APOGEE visits
e_v_rad	km s ⁻¹	Uncertainty in median radial-velocity
std_v_rad	km s ⁻¹	Radial-velocity scatter around the median.
cluster		Name of the star's host open cluster, as listed in Cantat-Gaudin et al. (2020) .
min_mjd	days	First Modified Julian Date of observation by SDSS.
max_mjd	days	Last Modified Julian Date of observation by SDSS.
n_total_visits		Total number of visits across all fields in SDSS III-V.
ruwe_threshold		Renormalized Unit Weight Error threshold for binarity, calculated using GAIAUNLIMITED.
ruwe		Gaia DR3 RUWE measurement
ruwe_binary	bool	Binary classification using only RUWE
delta_rv_max	km s ⁻¹	Maximum RV difference across all visits
delta_rv_max_binary	bool	Binary classification using only delta_rv_max.
joker_ln_total		JOKER log-likelihood from observed RV visits.
joker_ln_total_control		JOKER log-likelihood from synthetic normally distributed RV visits.
N_posterior_samples		Number of posterior samples returned by the JOKER.
joker_P	days	Best-fit period from the JOKER
joker_e		Best-fit eccentricity from the JOKER
joker_K	km s ⁻¹	Best-fit RV amplitude from the JOKER
ultranest_P	days	Best-fit period from ULTRANEST
ultranest_e		Best-fit eccentricity from ULTRANEST
ultranest_K	km s ⁻¹	Best-fit RV amplitude from ULTRANEST
joker_binary	bool	Binarity from ratio of joker_ln_total_control and joker_ln_total
binary	bool	Final binarity classification across all methods
unimodal	bool	Whether the star has a confident orbital solution
fm	M_\odot^2	Mass function calculated from stellar mass and orbital parameters.
orbital_m2	M_\odot	Minimum secondary mass assuming no inclination.
raw_teff	K	Uncalibrated effective temperature measured by ASPCAP.
iso_logg		Empirically derived surface gravity from raw_teff and interpolated EEP.
iso_vmicro	km s ⁻¹	Microturbulence calculated using iso_logg.
iso_mass	M_\odot	Present-day stellar mass from interpolated isochrone EEP.
iso_fe_h	dex	[Fe/H] from interpolated isochrone EEP.
iso_fe_chi2		χ^2 fit between iso_fe_h and observed spectrum.
bacchus_x_h	dex	[X/H] abundance from BACCHUS.
sp_e_x_h	dex	Uncertainty in [X/H] from atmospheric parameters.
line_e_x_h	dex	Line-to-line uncertainty in [X/H].
bacchus_e_x_h	dex	Total uncertainty in [X/H].

5.3 Chemical Variations versus Orbital Parameters

Previous studies in wide binaries, such as [Ramírez et al. \(2019\)](#) have shown a potential connection between abundance difference and orbital separation. We attempt to isolate a similar phenomenon in the close binary regime by checking for any correlation between chemical differences and orbital properties for the subset of binary stars with unimodal orbital solutions. We use each star's EEP, derived in

Section 4.1, to estimate the present-day stellar mass of the primary. Since none of our binaries have directly measured secondary masses or eclipses, we cannot fully solve the orbital solution. However, assuming an edge-on inclination angle ($\sin i = 1$) in Equation 5 below ([Kepler 1609](#)):

$$\frac{M_2^3 \sin^3 i}{(M_1 + M_2)^2} = \frac{PK^3}{2\pi G} (1 - e^2)^{3/2}, \quad (5)$$

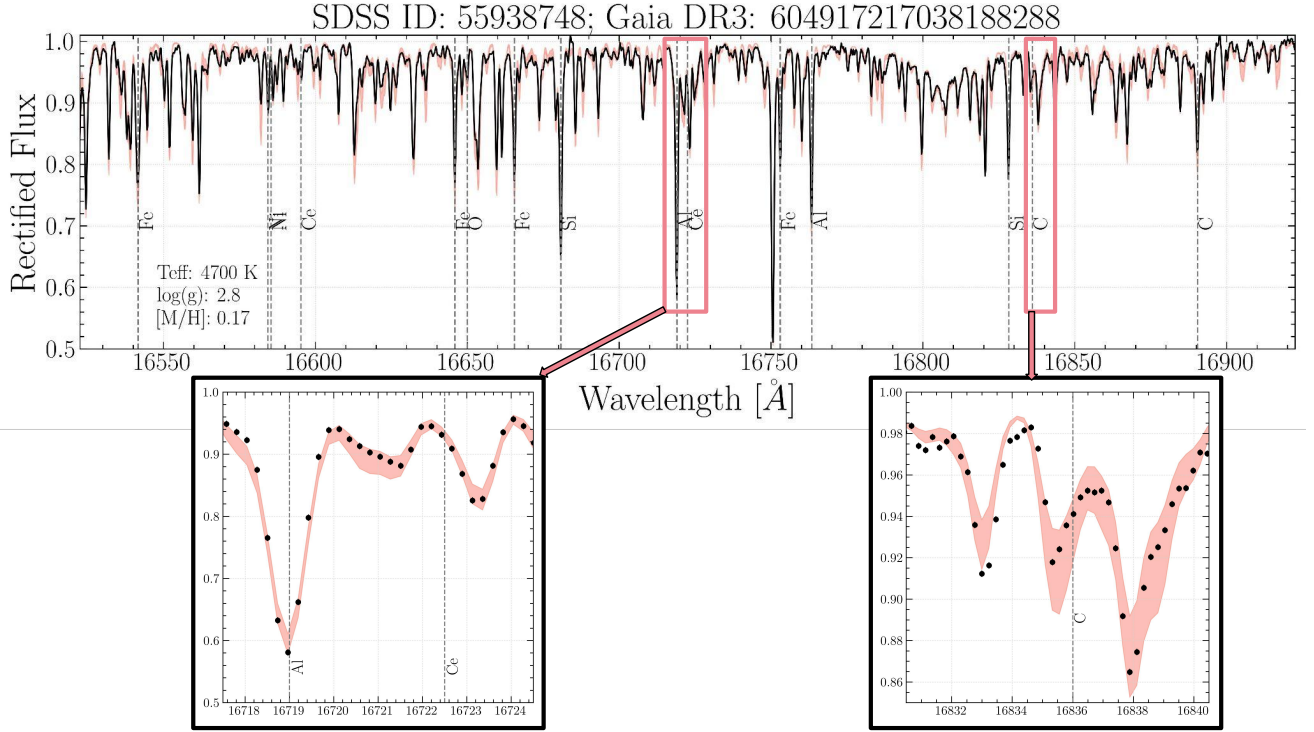


Figure 5. Here we show comparisons between the observed spectrum (black) and synthetic spectrum (salmon) for one of the stars in our sample, with our chosen absorption features shown as dashed lines (§4.2.1). We also show cutouts of two regions that contain C and Ce features to demonstrate the quality of our spectral synthesis. The shaded band shows a typical uncertainty in synthetic fit when considering the uncertainty in all the atmospheric parameters.

we can compute a minimum secondary mass ($M_{2,min}$) by solving Equation 5 as a straightforward cubic polynomial. We can also compute a minimum semi-major axis (a_{min})

$$a_{min} = \frac{P}{1 - e^2}, \quad (6)$$

and periastron (r_{min}), or point of closest approach:

$$r_{min} = \frac{P}{1 + e}. \quad (7)$$

As shown in Figure 8, we find that the orbital separations for unimodal binaries in our sample range between 10^{-1} and 10^1 astronomical units (AU). We measure the Spearman correlation between $\Delta[X/H]$, a_{min} , and r_{min} , and we find no relationship between any abundance difference and orbital separation. However, due to the strict selection criteria imposed by this analysis, we are very limited in sample size.

We also measure that the minimum periastrons are all larger than the Roche Lobe radii for the primaries in our binary sample, calculated using Equation 8, originally derived in Eggleton (1983):

$$\frac{r}{a_{min}} = \frac{0.49q^{2/3}}{0.6q^{2/3} + \ln(1 + q^{1/3})}. \quad (8)$$

Here q is the mass ratio $M_{2,min}/M_1$ and r is the Roche Lobe radius. While this result does not preclude the possibility of past mass transfer from the less luminous companion, in addition to orbital evolution, we cannot make predictions without independent constraints on the secondary masses.

6 DISCUSSION

6.1 [C/N] Comparison

Determining accurate stellar ages is a key area of interest in galactic archaeology. Knowing the ages of large sets of stars is crucial for understanding the Milky Way’s chemical composition and enrichment throughout its lifetime. The current gold standard for field star ages is via asteroseismology, through missions such as Kepler/K2 (Borucki et al. 2010; Howell et al. 2014), TESS (Ricker et al. 2015), CoRoT (Baglin et al. 2009a), and the upcoming PLATO and Roman missions (Baglin et al. 2009b; Roman Observations Time Allocation Committee & Core Community Survey Definition Committees 2025). However, there has also been significant work in so-called “chemical clocks”, or surface abundance ratios corresponding to stellar age (Espinoza-Rojas et al. 2021; Sales-Silva et al. 2022; Casali et al. 2025).

One commonly used chemical clock for stars on the red giant branch is the [C/N] ratio. This is because, as stars ascend the red giant branch, their convective envelopes expand and pull CNO-cycled material from above the core to the surface. As the amount of dredge-up is linked to stellar mass, the total surface [C/N] measured after a star begins its ascent on the RGB can be used as an age indicator (Masseron & Gilmore 2015; Martig et al. 2016; Spoo et al. 2022). Recent work has demonstrated that this method is viable for developing stellar age catalogues, and it can be informative for dating stars in the absence of other metrics (Stone-Martinez et al. 2025).

However, it has also been shown through works like Bufanda et al. (2023) and Frazer et al. (2025) that not all stars follow the expected [C/N]–mass relationship. While many potential causes have been

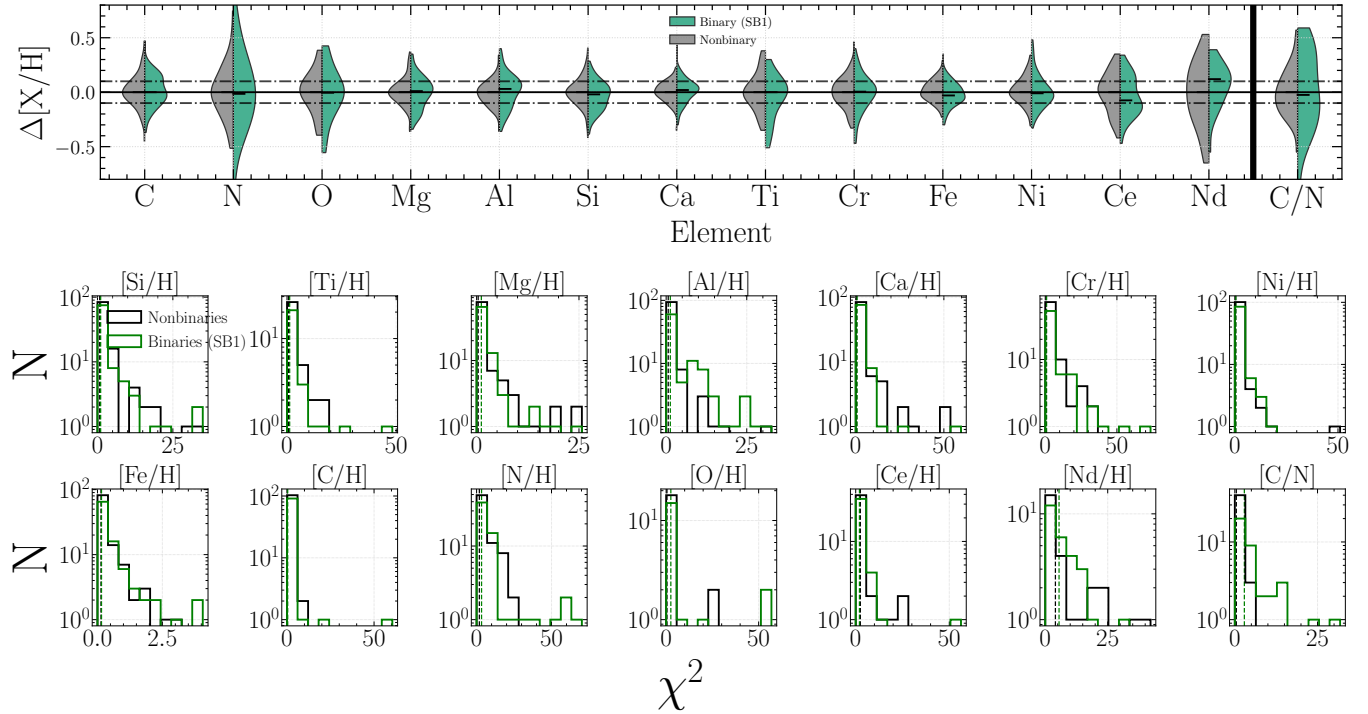


Figure 6. *Top:* Here we compare the $\Delta[X/H]$ and $\Delta[C/N]$ distributions for the SB1-nonbinary (green) and nonbinary-nonbinary (grey) pairs in all the elements we measure. The black lines indicate a $\Delta[X/H]$ of ± 0.1 dex. *Bottom:* Here we compare the elemental χ^2 distributions for the SB1-nonbinary (green) and nonbinary-nonbinary (grey) pairs in all the elements we measure. The black lines and green lines indicate the median nonbinary-nonbinary and median SB1-nonbinary χ^2 , respectively.

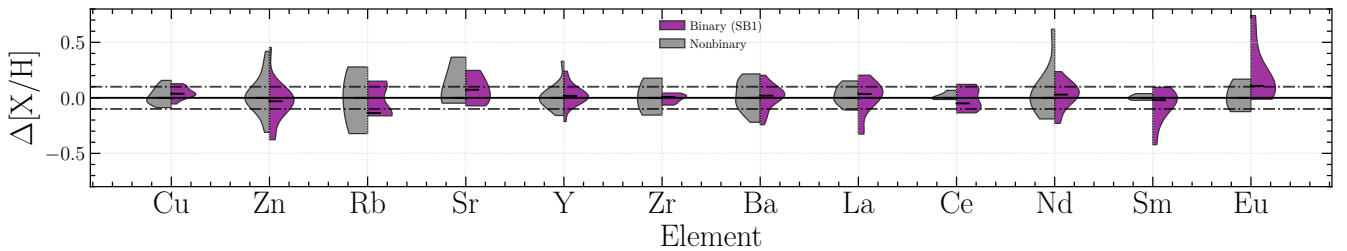


Figure 7. Similar to Figure 6 but for the neutron-capture elements for GALAH targets. The black lines indicate a $\Delta[X/H]$ of ± 0.1 dex.

proposed, including extra mixing and rotation, binary interactions leading to mass transfer is of particular interest to this paper (Lagarde et al. 2024; Carlberg et al. 2012; Tayar et al. 2015; Patton et al. 2024). In a close binary, if one member ascends the AGB before the other, it is possible that the binary would undergo a mass-transfer event, causing the less-evolved companion to become more massive. In addition, it is expected that both carbon and s-process elements like Ba or Ce would become enhanced in the less evolved star due to this mass transfer (Foster et al. 2024), with s-process enhancement larger than +0.3 dex, as noted in de Castro et al. (2016). The combination of these two effects would lead to unphysically ancient age measurements for observed stars (Spoo et al. 2022). One proposed method to study this has been to look for UV excess. Binaries that are brighter in the ultraviolet than expected have been shown to host white dwarfs (Anguiano et al. 2022); therefore, elevated [C/N] in UV-excess binaries is physically motivated and a potential indicator

of past mass transfer. In fact, in Frazer et al. (2025), the authors find APOKASC stars with GALEX UV excess as potential mass accretors. In a similar vein, Dixon et al. (2020) measure a relationship between RGB rapid rotators and NUV excess.

To examine this, we compare the $\Delta[C/N]$ measured between our binary-nonbinary and nonbinary-nonbinary sample as a function of UV excess, $\Delta(u-g)$, measured as the difference in $(u-g)$ colour between a binary and its matched single star. We find a potential relationship between binaries with UV excess and $\Delta[C/N]$, as shown in Figure 9. In particular, we find that binary members with significant UV excess exhibit a 0.2–0.5 dex increase in [C/N]. However, none of these UV excess binaries show enhancement in Ce or Nd ($\Delta[Ce/H] < 0.2$), and all have $v \sin i \leq 7 \text{ km s}^{-1}$, so further study is needed to confirm whether this relationship is truly caused by close proximity to a white dwarf.

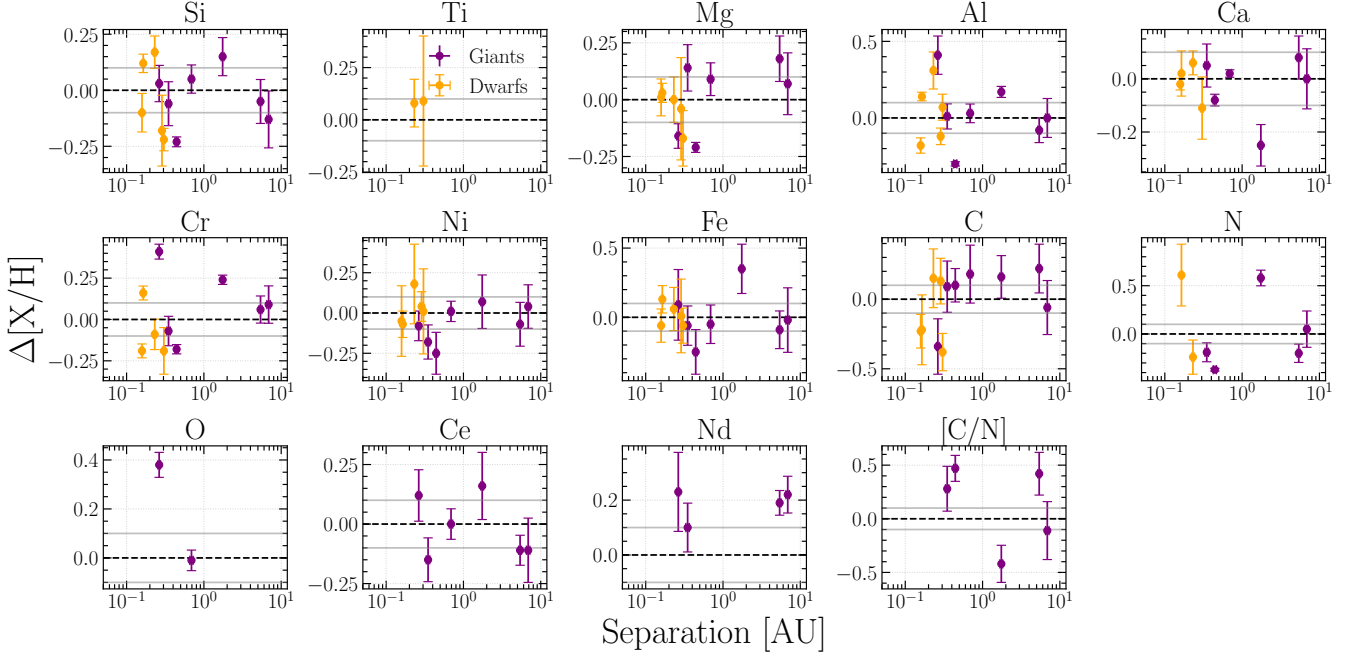


Figure 8. Here we show the measured semi-major axis as orbital separation, compared to $\Delta[X/H]$, for unimodal binaries with a nonbinary counterpart at similar temperature and surface gravity (Section 5.1). We do not find any trend between orbital parameter and surface abundance difference. Giant stars are shown in purple and dwarf stars are shown in orange.

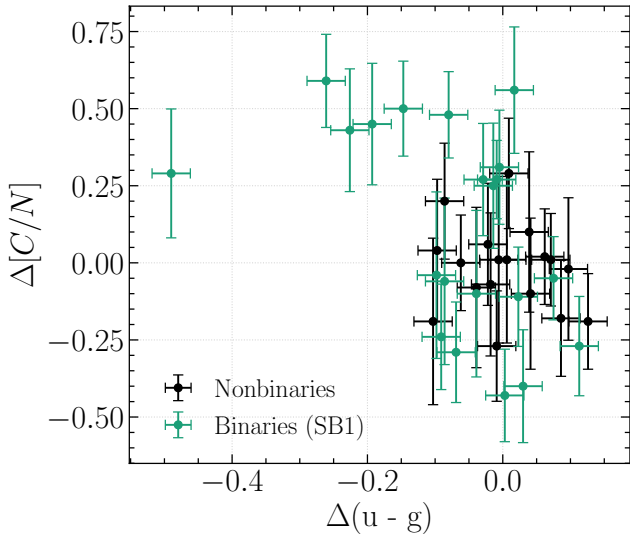


Figure 9. Here we show $\Delta[C/N]$ as a function of $\Delta(u - g)$. SB1 primaries with large UV excess have significant increases in $[C/N]$, and thus increases in the age that would be measured with that abundance.

6.2 Chemical Homogeneity of Close Binaries in a Galactic Context

Understanding how elements are dispersed from their production sites throughout the Milky Way, and the different mixing lengths for each nucleosynthetic pathway, is central to galactic archaeology. One of the ways we study these processes is through the variation in chemical abundances at different spatial scales. Previous work has

shown that Milky Way field stars at similar ages, galactocentric radii, $[M/H]$, and $[a/M]$ have a ~ 0.2 dex dispersion in chemical abundances (Hayden et al. 2015; Ness et al. 2018). On the other hand, co-natal stellar populations, such as open clusters, have dispersions of ≤ 0.1 dex (e.g., Bovy 2016; Poovelil et al. 2020; Ness et al. 2022; Sinha et al. 2024). As the basic building blocks of the Milky Way, the dissolution of these clusters populates the disc and bar/bulge with stars. Understanding the spatial correlation between co-eval stars and chemical homogeneity can inform us how elements are mixed throughout the Galaxy.

In this section and Figure 10, we collect results from previous literature to investigate the relationship between chemical homogeneity and physical scales in the Milky Way. To accomplish this, we compare the binary-nonbinary homogeneity measured in Section 5 to the chemical homogeneity between pairs of open cluster stars, the intra-pair homogeneity of wide binaries and co-moving stars, and finally co-eval field stars at increasing separations within the disc. For separations smaller than 10^6 AU, we require a minimum of three pairs per bin, resulting in unequal spacing. At separations larger than 10^6 AU, we use bins with separations of 0.35 in $\log(\text{AU})$ space, and all bins in this regime contain $N \gg 3$ pairs.

With separations between 10^3 and 10^5 astronomical units, wide binaries are the next step up from close binaries on the distance ladder of co-eval and co-natal stars. Previous studies of wide binary chemistry, such as Andrews et al. (2018, 2019); Hawkins et al. (2020); Lim et al. (2024), have found that they are homogeneous within 0.05 dex across a broad suite of elements. We compare the $\Delta[X/H]$ distributions of our unimodal binaries to the results of Hawkins et al. (2020), and find that our SB1s exhibit a similar level of chemical similarity to previous studies of wide binaries. We note, though, that the metrics for $\Delta[X/H]$ are slightly different between the wide and close binaries. Our SB1s are being compared to nonbinaries, in the

same cluster at the same effective temperature and surface gravity, with the idea that the nonbinary stars are a benchmark for the SB1 primary. In [Hawkins et al. \(2020\)](#), since both binary members are resolvable on the sky, they can measure the intra-pair $\Delta[X/H]$ directly. Figure 10 does not include any wide binary data for $\Delta[\text{Ce}/\text{H}]$ as [Hawkins et al. \(2020\)](#) did not measure Ce in their analysis.

With separations between 10^4 and 10^5 astronomical units, nonbinaries in open clusters are the largest sample of co-eval/co-natal stars that are not in a binary. We measure the spatial separation for all the nonbinary-nonbinary pairs assembled in Section 5.1. We find that their dispersion in $[\text{Fe}/\text{H}]$ is ~ 0.1 dex, which is in agreement with previous literature on open cluster abundance dispersion ([De Silva et al. 2007](#); [Bovy 2016](#); [Sinha et al. 2024](#); [Grilo et al. 2024](#)).

Lastly, we use co-moving pairs from [Kamdar et al. \(2019\)](#) and [Nelson et al. \(2021\)](#) to study the chemical similarity of co-natal pairs between 10^5 and 10^7 AU. Both studies found that co-moving pairs of stars were chemically homogeneous in $[\text{Fe}/\text{H}]$ within 0.1 dex. While [Kamdar et al. \(2019\)](#) did not measure the intra-pair abundance difference for any other element, [Nelson et al. \(2021\)](#) measured $\Delta[X/H]$ for two dozen elements, including Mg and Nd.

We compare our sample of binaries to a set of co-eval, but not co-natal, field stars in the Milky Way. Using the MWM DR19 StarFlow Value Added catalogue¹⁰ of stellar masses and ages ([Stone-Martinez et al. 2025](#)), we apply the same quality cuts outlined in Section 2, resulting in a sample of $\sim 31,000$ stars. Using the same binary selection methods outlined in 3, as well as a threshold of seven radial velocity visits, we identify $\sim 12,000$ binaries and $\sim 19,000$ nonbinaries in this field star sample. Finally, for the reasons outlined in 4.2, we use Ce and Nd measurements for stars on the giant branch.

Using GALPY ([Bovy 2015a](#)), we integrate the orbits of the StarFlow sample using the `MWPotential2014` gravitational potential ([Mackereth & Bovy 2018](#)) in order to determine each star's guiding radius (R_{guide}). Finally, we pair field stars in the StarFlow sample with their closest match in age, temperature, and surface gravity, where we use the same temperature and surface gravity thresholds as in Section 5.1. Stars without a match within the temperature and surface gravity thresholds were removed from the sample.

We measure the difference in R_{guide} within each pair and take that as the separation between the two stars, finding field star separations span 0.6 and 9.5 kpc, with an average uncertainty of ~ 0.1 kpc.

Finally, we measure the intra-pair $\Delta[X/H]$ for all our field star pairs within four chemical species: $[\text{Fe}/\text{H}]$, $[\text{Mg}/\text{H}]$, $[\text{Ce}/\text{H}]$, and $[\text{Nd}/\text{H}]$. These four were chosen as they all trace different nucleosynthetic pathways, informing us about the iron-peak (Fe), alpha- (Mg), and neutron-capture (Nd and Ce) pathways.

Between our sample of open cluster SB1s and nonbinaries, wide binaries from [Hawkins et al. \(2020\)](#), and matched field stars from StarFlow, we have a large sample of ostensibly co-eval pairs that are increasingly less co-natal. From this dataset, we measure the $\sigma_{\Delta[X/H]}$ as a function of separation in order to quantify the relationship between intra-pair homogeneity and spatial separation. The results of this are shown in Figure 10. With the potential exception of Nd, at all separations smaller than one parsec, $\sigma_{\Delta[X/H]}$ is ≤ 0.1 dex across all the different nucleosynthetic tracers.

While the dispersion in $\sigma_{\Delta[\text{Nd}/\text{H}]}$ appears to increase to ~ 0.3 dex at 10^4 AU, this is less likely to be driven by astrophysical mechanisms, and more due to the limited sample of stars with $\Delta[\text{Nd}/\text{H}]$ measurements at that separation. This hypothesis is strengthened by the

fact that Ce follows similar enrichment pathways to Nd, but has more measurements at 10^4 AU, and $\sigma_{\Delta[\text{Ce}/\text{H}]}$ is consistent with homogeneity at 10^4 AU. Furthermore, when using only results from [Hawkins et al. \(2020\)](#), we find $\sigma_{\Delta[\text{Nd}/\text{H}]} \leq 0.1$ dex at similar separations.

The fact that within one pc we measure a $\sigma_{\Delta[X/H]}$ consistent with homogeneity implies that at distances smaller than one pc, gas is being mixed homogeneously enough that there is no statistical difference in surface abundance, which is consistent with results from simulations ([Armillotta et al. 2018](#); [Kolborg et al. 2022](#); [Krumholz et al. 2025](#)). Equally interesting, though, is the fact that beyond one pc of separation, even when controlling for factors such as age, temperature, and surface gravity, we find an immediate increase in $\sigma_{\Delta[X/H]}$. Within separations of 1 kpc, we find that the dispersion in light element and neutron-capture channels are ~ 0.2 dex and ~ 0.35 dex respectively, which is in agreement with previous findings ([Ness et al. 2022](#); [Manea et al. 2024](#)).

Important throughout this analysis is the result that at all scales between 10^{-1} and 10^7 AU, there is no statistical difference in the chemical homogeneity of co-natal and co-eval pairs of stars across any nucleosynthetic channel. Given that at all scales below one pc, n-capture elements appear as homogeneous as the light elements, larger dispersions than the light elements at larger separations imply they are potentially being mixed differently into the ISM. Therefore, as also noted by [Manea et al. \(2025\)](#), n-capture elements are far more suited to distinguish co-natal populations dissolved in the field than the lighter elements.

7 CONCLUSIONS

The purpose of this study was to measure the chemistry of SB1 primaries in order to determine how close binarity can affect surface abundances. To accomplish this, we determine the SB1 membership of 14 open clusters in SDSS-V Milky Way Mapper DR19 using a combination of radial velocities and Gaia DR3 RUWE. Within our open cluster sample, we identify 119 likely-single stars and 103 likely-SB1s with FGK primaries. Only 16 targets in our sample of likely binaries have well-constrained orbital parameters.

To study the difference between binaries and nonbinaries as a population, we measure the $\Delta[X/H]$ between binaries and nonbinaries at similar effective temperatures and surface gravities. We verify, and re-derive where necessary, the atmospheric parameters for all the stars in our sample. Using MWM DR19 spectra and the BACCHUS spectral synthesis code, we re-derive abundances in the following 13 elements, as well as the $[\text{C}/\text{N}]$ ratio: Si, Fe, C, N, O, Na, Mg, Al, Ca, Ti, Cr, Ni, Ce, and Nd.

From this analysis, we find the following:

- (i) Compared to a non-binary baseline using a K-S test, we find no statistical difference between the two populations across all the elements we studied.
- (ii) When crossmatched to GALAH DR4 to study potential neutron-capture variations, we still find no statistical difference in $\Delta[X/H]$ between the binary-nonbinary and nonbinary-nonbinary populations.
- (iii) We measure the relationship between $\Delta[X/H]$ and orbital parameter for the sample of SB1s for which we have constrained orbital solutions. We find no trend in abundance difference between 10^{-1} and 10^1 AU.
- (iv) Though there is no statistical difference between the binary-nonbinary and nonbinary-nonbinary $\Delta[\text{C}/\text{N}]$ as a whole population, we do find a trend when measuring the relationship between UV excess and $\Delta[\text{C}/\text{N}]$. We find that binary stars with UV excess have an enhanced $[\text{C}/\text{N}]$ ratio compared to single stars of comparable mass.

¹⁰ https://www.sdss.org/dr19/data_access/value-added-catalogues/?vac_id=10003

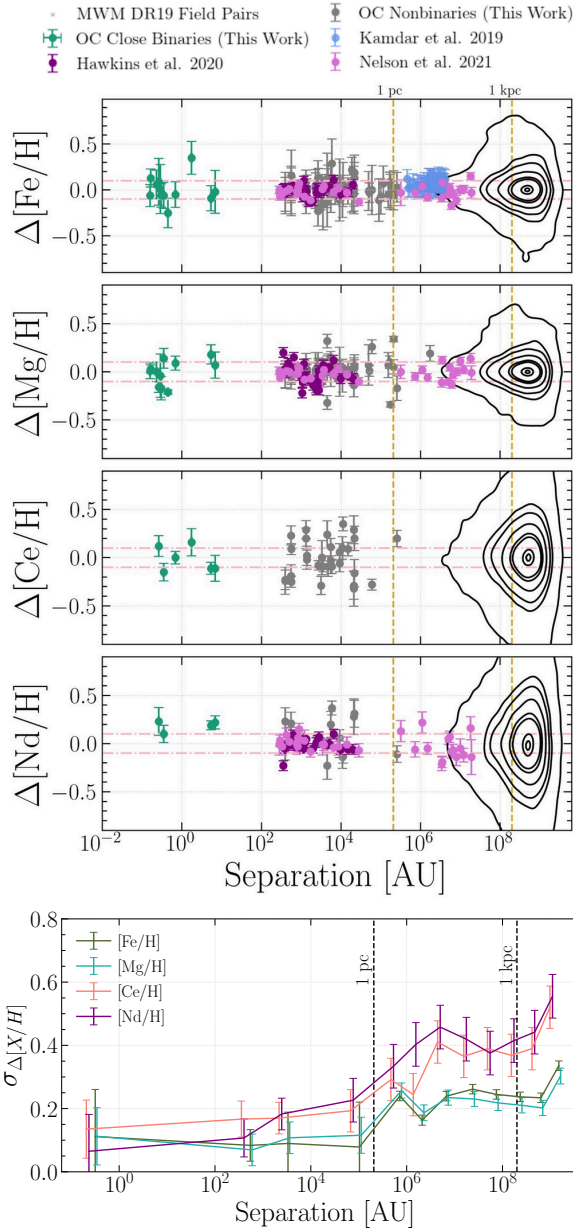


Figure 10. *Top:* Here we compare the $\Delta[X/H]$ distributions for the binary-nonbinary co-eval stars at increasing separations across four elements: Fe, Mg, Ce, and Nd. We note that the plot for $\Delta[\text{Ce}/\text{H}]$ does not include any wide binaries or co-moving pairs as Hawkins et al. (2020) and Nelson et al. (2021) did not measure Ce in their analyses. *Bottom:* We find that below separations of 1 pc, stars can be considered chemically homogeneous across all nucleosynthetic channels. Beyond one pc but within one kpc, there is a sudden increase in $\sigma_{\Delta[X/H]}$, with the light and heavy elements separating into two different tracks. Lastly, at separations beyond one kpc, $\sigma_{\Delta[X/H]}$ steadily increases. We show contours for the 5th, 25th, 34th, 50th, 68th, 75th, and 95th percentiles for the top four panels.

We find that $[\text{C}/\text{N}]$ can be enhanced between 0.2–0.5 dex, which corresponds to an increase in the inferred $\log(\text{age})_{[\text{C}/\text{N}]}$ by up to ~ 1 dex. This overestimation in age has implications for the efficacy of $[\text{C}/\text{N}]$ as a chemical clock for red giant stars, underscoring the importance of considering binarity when measuring stellar ages.

- (v) We find that at separations of 1 pc or less, co-eval stars can be considered chemically homogeneous across all nucleosynthetic channels.

However, at separations beyond one pc, we see the dispersion in $\Delta[X/H]$ increases at different rates for the light and neutron-capture elements. This difference in dispersion implies that elements from these nucleosynthetic channels are being mixed from their production sites into the broader Galaxy through different means. This also strongly supports the idea that neutron-capture elements are far more useful at identifying co-natal populations than the lighter elements.

ACKNOWLEDGEMENTS

We would like to thank the referee for their helpful comments, which have improved this analysis. A.S. would also like to acknowledge Shelly S. for her helpful conversations and who sadly passed away prior to this work’s publication. This material is based upon work supported by the National Science Foundation under Grant No. AST-2206542. K.C. acknowledges support from NSF Grant No. AST-2206543. D.S. acknowledges support from the Foundation for Research and Technological Innovation Support of the State of Sergipe (FAPITEC/SE) and the National Council for Scientific and Technological Development (CNPq), under grant numbers 404056/2021-0, 794017/2013, and 444372/2024-5. J.C. acknowledges support from the Agencia Nacional de Investigación y Desarrollo (ANID) via Proyecto Fondecyt Regular 1231345, and by ANID BASAL project FB210003.

Funding for the Sloan Digital Sky Survey V has been provided by the Alfred P. Sloan Foundation, the Heising-Simons Foundation, the National Science Foundation, and the Participating Institutions. SDSS acknowledges support and resources from the Center for High-Performance Computing at the University of Utah. SDSS telescopes are located at Apache Point Observatory, funded by the Astrophysical Research Consortium and operated by New Mexico State University, and at Las Campanas Observatory, operated by the Carnegie Institution for Science. The SDSS web site is www.sdss.org.

SDSS is managed by the Astrophysical Research Consortium for the Participating Institutions of the SDSS Collaboration, including the Carnegie Institution for Science, Chilean National Time Allocation Committee (CNTAC) ratified researchers, Caltech, the Gotham Participation Group, Harvard University, Heidelberg University, The Flatiron Institute, The Johns Hopkins University, L’Ecole polytechnique fédérale de Lausanne (EPFL), Leibniz-Institut für Astrophysik Potsdam (AIP), Max-Planck-Institut für Astronomie (MPIA Heidelberg), Max-Planck-Institut für Extraterrestrische Physik (MPE), Nanjing University, National Astronomical Observatories of China (NAOC), New Mexico State University, The Ohio State University, Pennsylvania State University, Smithsonian Astrophysical Observatory, Space Telescope Science Institute (STScI), the Stellar Astrophysics Participation Group, Universidad Nacional Autónoma de México, University of Arizona, University of Colorado Boulder, University of Illinois at Urbana-Champaign, University of Toronto, University of Utah, University of Virginia, Yale University, and Yunnan University.

SOFTWARE

ASTROPY (Astropy Collaboration et al. 2013, 2018, 2022), SCIPY (Virtanen et al. 2020), MATPLOTLIB (Hunter 2007), NUMPY (Harris et al. 2020), PANDAS (pandas development team 2020; Wes McKinney 2010), ISOCHRONES (Morton 2015), GALPY (Bovy 2015b), BACCHUS_TOOLS, and PYBACCHUS (Sinha 2025).

DATA AVAILABILITY

The data for this project is publicly available through SDSS-V and the Gaia Collaboration. SDSS-V spectra and radial velocities can be found here (https://www.sdss.org/dr19/data_access/), and instructions on how to query the Gaia main_table as well as NSS catalogue can be found here (<https://www.cosmos.esa.int/web/gaia/dr3>). The cluster membership, atmospheric parameters, binary membership, and elemental abundances derived from this analysis will be made available as a machine-readable table.

REFERENCES

- Abdurro'uf et al., 2022, *ApJS*, 259, 35
- Almeida A., et al., 2023, *ApJS*, 267, 44
- Andrews J. J., Chanamé J., Agüeros M. A., 2018, *MNRAS*, 473, 5393
- Andrews J. J., Anguiano B., Chanamé J., Agüeros M. A., Lewis H. M., Hayes C. R., Majewski S. R., 2019, *ApJ*, 871, 42
- Anguiano B., et al., 2022, *AJ*, 164, 126
- Armillotta L., Krumholz M. R., Fujimoto Y., 2018, *MNRAS*, 481, 5000
- Astropy Collaboration et al., 2013, *A&A*, 558, A33
- Astropy Collaboration et al., 2018, *AJ*, 156, 123
- Astropy Collaboration et al., 2022, *apj*, 935, 167
- Badenes C., et al., 2018, *ApJ*, 854, 147
- Baglin A., Auvergne M., Barge P., Deleuil M., Michel E., CoRoT Exoplanet Science Team 2009a, in Pont F., Sasselov D., Holman M. J., eds, IAU Symposium Vol. 253, Transiting Planets. pp 71–81, doi:10.1017/S1743921308026252
- Baglin A., Auvergne M., Barge P., Deleuil M., Michel E., CoRoT Exoplanet Science Team 2009b, in Pont F., Sasselov D., Holman M. J., eds, IAU Symposium Vol. 253, Transiting Planets. pp 71–81, doi:10.1017/S1743921308026252
- Barkhouser R. H., et al., 2022, in Marshall H. K., Spyromilio J., Usuda T., eds, Society of Photo-Optical Instrumentation Engineers (SPIE) Conference Series Vol. 12182, Ground-based and Airborne Telescopes IX. p. 1218230, doi:10.1117/12.2630655
- Bidelman W. P., Keenan P. C., 1951, *ApJ*, 114, 473
- Blanton M. R., et al., 2017, *AJ*, 154, 28
- Borucki W. J., et al., 2010, *Science*, 327, 977
- Bovy J., 2015a, *ApJS*, 216, 29
- Bovy J., 2015b, *ApJS*, 216, 29
- Bovy J., 2016, *ApJ*, 817, 49
- Bowen I. S., Vaughan A. H. J., 1973, *Appl. Opt.*, 12, 1430
- Buder S., et al., 2021, *MNRAS*, 506, 150
- Buder S., et al., 2025, *Publ. Astron. Soc. Australia*, 42, e051
- Bufanda E., Tayar J., Huber D., Hesselquist S., Lane R. R., 2023, *ApJ*, 959, 123
- Cantat-Gaudin T., et al., 2020, *A&A*, 640, A1
- Carlberg J. K., Cunha K., Smith V. V., Majewski S. R., 2012, *ApJ*, 757, 109
- Casagrande L., Ramírez I., Meléndez J., Bessell M., Asplund M., 2010, *A&A*, 512, A54
- Casali G., et al., 2025, *MNRAS*, 541, 2631
- Castro-Ginard A., et al., 2024, *A&A*, 688, A1
- Castro-Tapia M., Aguilera-Gómez C., Chanamé J., 2024, *A&A*, 690, A367
- Cheng C. M., Price-Jones N., Bovy J., 2021, *MNRAS*, 506, 5573
- Choi J., Dotter A., Conroy C., Cantiello M., Paxton B., Johnson B. D., 2016, *ApJ*, 823, 102
- Cseh B., et al., 2018, *A&A*, 620, A146
- Cunha K., et al., 2017, *ApJ*, 844, 145
- De Silva G. M., Freeman K. C., Asplund M., Bland-Hawthorn J., Bessell M. S., Collet R., 2007, *AJ*, 133, 1161
- Dixon D., Tayar J., Stassun K. G., 2020, *AJ*, 160, 12
- Dotter A., 2016, *ApJS*, 222, 8
- Duchêne G., Kraus A., 2013, *ARA&A*, 51, 269
- Eggleton P. P., 1983, *ApJ*, 268, 368
- Eisenstein D. J., et al., 2011, *AJ*, 142, 72
- El-Badry K., Rix H.-W., Heintz T. M., 2021, *MNRAS*, 506, 2269
- Espinoza-Rojas F., Chanamé J., Jofré P., Casamiquela L., 2021, *ApJ*, 920, 94
- Foster S., et al., 2024, *A&A*, 689, A230
- Frazer P., Griffith E. J., Hogg D. W., Sinha A., Tayar J., 2025, *arXiv e-prints*, p. arXiv:2510.26927
- Gaia Collaboration et al., 2023a, *A&A*, 674, A1
- Gaia Collaboration et al., 2023b, *A&A*, 674, A34
- García Pérez A. E., et al., 2016, *AJ*, 151, 144
- Geller A. M., Mathieu R. D., Latham D. W., Pollack M., Torres G., Leiner E. M., 2021, *AJ*, 161, 190
- Gizis J., Reid I., 1997, *PASP*, 109, 1232
- Grevesse N., Asplund M., Sauval A. J., 2007, *Space Sci. Rev.*, 130, 105
- Grilo V., et al., 2024, *MNRAS*, 534, 3005
- Gunn J. E., et al., 2006, *AJ*, 131, 2332
- Gustafsson B., Edvardsson B., Eriksson K., Jørgensen U. G., Nordlund Å., Plez B., 2008, *A&A*, 486, 951
- Harris C. R., et al., 2020, *Nature*, 585, 357
- Hasselquist S., et al., 2016, *ApJ*, 833, 81
- Hawkins K., et al., 2016, *A&A*, 592, A70
- Hawkins K., et al., 2020, *MNRAS*, 492, 1164
- Hayden M. R., et al., 2015, *ApJ*, 808, 132
- Hayes C. R., et al., 2022, *ApJS*, 262, 34
- Howell S. B., et al., 2014, *PASP*, 126, 398
- Hunt E. L., Reffert S., 2023, VizieR Online Data Catalog, ppJ/A+A/673/A114
- Hunter J. D., 2007, *Computing in Science & Engineering*, 9, 90
- Jorissen A., Boffin H. M. J., Karinkuzhi D., Van Eck S., Escorza A., Shetye S., Van Winckel H., 2019, *A&A*, 626, A127
- Kamdar H., Conroy C., Ting Y.-S., Bonaca A., Smith M. C., Brown A. G. A., 2019, *ApJ*, 884, L42
- Kepler J., 1609, *Astronomia nova*.
- Kolborg A. N., Martizzi D., Ramirez-Ruiz E., Pfister H., Sakari C., Wechsler R. H., Soares-Furtado M., 2022, *ApJ*, 936, L26
- Kollmeier J. A., et al., 2017, *arXiv e-prints*, p. arXiv:1711.03234
- Kollmeier J. A., et al., 2025, *arXiv e-prints*, p. arXiv:2507.06989
- Kounkel M., et al., 2021, *AJ*, 162, 184
- Krumholz M. R., Ting Y.-S., Li Z., Zhang C., Mead J., Ness M. K., 2025, *arXiv e-prints*, p. arXiv:2507.14572
- Lada C. J., Lada E. A., 2003, *ARA&A*, 41, 57
- Lagarde N., et al., 2024, *A&A*, 684, A70
- Lim D., Koch-Hansen A. J., Hong S., Chun S.-H., Lee Y.-W., 2024, *AJ*, 167, 3
- Lugaro M., Herwig F., Lattanzio J. C., Gallino R., Straniero O., 2003, *ApJ*, 586, 1305
- Lugaro M., Pignatari M., Reifarth R., Wiescher M., 2023, *Annual Review of Nuclear and Particle Science*, 73, 315
- Mack III C. E., Stassun K. G., Schuler S. C., Hebb L., Pepper J. A., 2016, *ApJ*, 818, 54
- Mackereth J. T., Bovy J., 2018, *PASP*, 130, 114501
- Manea C., Hawkins K., Ness M. K., Buder S., Martell S. L., Zucker D. B., 2024, *ApJ*, 972, 69
- Manea C., et al., 2025, *arXiv e-prints*, p. arXiv:2508.16717
- Martig M., et al., 2016, *MNRAS*, 456, 3655
- Martín E. L., Basri G., Pavlenko Y., Lyubchik Y., 2002, *ApJ*, 579, 437
- Masseron T., Gilmore G., 2015, *MNRAS*, 453, 1855
- Masseron T., Merle T., Hawkins K., 2016, BACCHUS: Brussels Automatic Code for Characterizing High accuracy Spectra, Astrophysics Source Code Library, record ascl:1605.004
- Masseron T., et al., 2019, *A&A*, 622, A191
- Mathieu R. D., 2000, in Pallavicini R., Micela G., Sciortino S., eds, Astronomical Society of the Pacific Conference Series Vol. 198, Stellar Clusters and Associations: Convection, Rotation, and Dynamos. p. 517
- Mészáros S., et al., 2025, *arXiv e-prints*, p. arXiv:2506.07845
- Michaud G., Alecian G., Richer J., 2015, *Atomic Diffusion in Stars*, doi:10.1007/978-3-319-19854-5.
- Moe M., Kratter K. M., Badenes C., 2019, *ApJ*, 875, 61
- Morton T. D., 2015, isochrones: Stellar model grid package, Astrophysics Source Code Library, record ascl:1503.010 (ascl:1503.010)

- Müller-Horn J., Rix H.-W., El-Badry K., Pennell B., Green M., Li J., Seeburger R., 2025a, *arXiv e-prints*, p. [arXiv:2510.05982](https://arxiv.org/abs/2510.05982)
- Müller-Horn J., Göttgens F., Dreizler S., Kamann S., Martens S., Saracino S., Ye C. S., 2025b, *A&A*, **693**, A161
- Nelson T., Ting Y.-S., Hawkins K., Ji A., Kamdar H., El-Badry K., 2021, *ApJ*, **921**, 118
- Ness M., et al., 2018, *ApJ*, **853**, 198
- Ness M. K., Wheeler A. J., McKinnon K., Horta D., Casey A. R., Cunningham E. C., Price-Whelan A. M., 2022, *ApJ*, **926**, 144
- Offner S. S. R., Kratter K. M., Matzner C. D., Krumholz M. R., Klein R. I., 2010, *ApJ*, **725**, 1485
- Offner S. S. R., Moe M., Kratter K. M., Sadavoy S. I., Jensen E. L. N., Tobin J. J., 2023, in Inutsuka S., Aikawa Y., Muto T., Tomida K., Tamura M., eds, *Astronomical Society of the Pacific Conference Series Vol. 534, Protostars and Planets VII*. p. 275 ([arXiv:2203.10066](https://arxiv.org/abs/2203.10066)), doi:10.48550/arXiv.2203.10066
- Otto J. M., et al., 2026, *AJ*, **171**, 91
- Patton R. A., et al., 2024, *MNRAS*, **528**, 3232
- Paxton B., Bildsten L., Dotter A., Herwig F., Lesaffre P., Timmes F., 2011, *ApJS*, **192**, 3
- Plez B., 2012, *Turbospectrum: Code for spectral synthesis*, Astrophysics Source Code Library, record ascl:1205.004 (ascl:1205.004)
- Pogge R. W., et al., 2020, in Evans C. J., Bryant J. J., Motohara K., eds, *Society of Photo-Optical Instrumentation Engineers (SPIE) Conference Series Vol. 11447, Ground-based and Airborne Instrumentation for Astronomy VIII*. p. 1144781, doi:10.1117/12.2561113
- Poovelil V. J., et al., 2020, *ApJ*, **903**, 55
- Prantzos N., Abia C., Cristallo S., Limongi M., Chieffi A., 2020, *MNRAS*, **491**, 1832
- Price-Whelan A. M., et al., 2020, *ApJ*, **895**, 2
- Prša A., et al., 2016, *AJ*, **152**, 41
- Ramírez I., Khanal S., Lichon S. J., Chanamé J., Endl M., Meléndez J., Lambert D. L., 2019, *MNRAS*, **490**, 2448
- Ramos A. A., Holanda N., Drake N. A., Rain M. J., Maia F. F. S., Daflon S., Pereira C. B., 2024, *MNRAS*, **527**, 6211
- Ricker G. R., et al., 2015, *Journal of Astronomical Telescopes, Instruments, and Systems*, **1**, 014003
- Roman Observations Time Allocation Committee Core Community Survey Definition Committees 2025, *arXiv e-prints*, p. [arXiv:2505.10574](https://arxiv.org/abs/2505.10574)
- SDSS Collaboration et al., 2025, *arXiv e-prints*, p. [arXiv:2507.07093](https://arxiv.org/abs/2507.07093)
- Sales-Silva J. V., et al., 2022, *ApJ*, **926**, 154
- Sandage A. R., 1953, *AJ*, **58**, 61
- Shroyer J. E., Carlberg J., 2020, in *American Astronomical Society Meeting Abstracts #235*. p. 110.20
- Sinha A., 2025, *PyBACCHUS: A Python Wrapper for running the Brussels Automatic Code for Characterizing High accuracy Spectra (BACCHUS)*, doi:10.5281/zenodo.17070806, <https://github.com/rocketxturtle/PyBACCHUS>
- Sinha A., Zasowski G., Frinchaboy P., Cunha K., Souto D., Tayar J., Stassun K., 2024, *ApJ*, **975**, 89
- Skrutskie M. F., et al., 2006, *AJ*, **131**, 1163
- Smith V. V., et al., 2021, *AJ*, **161**, 254
- Snedden C., 1973, *ApJ*, **184**, 839
- Souto D., et al., 2019, *ApJ*, **874**, 97
- Spoo T., et al., 2022, *AJ*, **163**, 229
- Stebbins J., 1911, *ApJ*, **34**, 105
- Stone-Martinez A., Holtzman J. A., Lu Y., Hasselquist S., Imig J., Griffith E. J., Bellinger E. P., Saydjari A. K., 2025, *AJ*, **170**, 66
- Sun M., Mathieu R. D., Leiner E. M., Townsend R. H. D., 2021, *ApJ*, **908**, 7
- Tayar J., et al., 2015, *ApJ*, **807**, 82
- Van der Swaelmen M., Boffin H. M. J., Jorissen A., Van Eck S., 2017, *A&A*, **597**, A68
- Vejar G., Schuler S. C., Stassun K. G., 2021, *ApJ*, **919**, 100
- Virtanen P., et al., 2020, *Nature Methods*, **17**, 261
- Wes McKinney 2010, in Stéfan van der Walt Jarrod Millman eds, *Proceedings of the 9th Python in Science Conference*. pp 56 – 61, doi:10.25080/Majora-92bf1922-00a
- Wheeler A. J., Abruzzo M. W., Casey A. R., Ness M. K., 2023, *AJ*, **165**, 68
- Wilson J. C., et al., 2019, *PASP*, **131**, 055001
- de Castro D. B., Pereira C. B., Roig F., Jilinski E., Drake N. A., Chavero C., Sales Silva J. V., 2016, *MNRAS*, **459**, 4299
- de Medeiros J. R., Da Rocha C., Mayor M., 1996, *A&A*, **314**, 499
- pandas development team T., 2020, *pandas-dev/pandas: Pandas*, doi:10.5281/zenodo.3509134, <https://doi.org/10.5281/zenodo.3509134>

This paper has been typeset from a $\text{\TeX}/\text{\LaTeX}$ file prepared by the author.